

## AN ABSTRACT OF THE THESIS OF

Neil Roberts for the degree of Doctor of Philosophy in Physics presented on  
December 3, 2004.

Title: NMR of Novel Oxides

Abstract approved:

Redacted for Privacy

WILLIAM W. WALLICH, JR.

We report  $^{27}\text{Al}$  and  $^{69,71}\text{Ga}$  impurity and  $^{67}\text{Zn}$  host species NMR experiments on ZnO powders containing Al or Ga dopants in the range 0.03 to 3 at. %. Spectral analysis of the  $^{67}\text{Zn}$  and  $^{69}\text{Ga}$  quadrupole powder patterns indicate gallium is substitutional for zinc and the electric quadrupole coupling of dilute  $^{69}\text{Ga}$  is determined to be  $(e^2qQ/h)_{69} = 3.9 \pm 0.3 \text{ MHz}$ . Resonant shift data and spin-lattice relaxation rates are reduced to yield values for impurity chemical and Knight shifts. The data are correlated by the Korringa relation throughout the impurity concentration range indicating nearly ideal metallic behavior, where exchange and correlation effects are absent in the conduction electron system. Temperature dependent studies of the spin-lattice relaxation rate are consistent with coupling of a degenerate electron system to nuclear magnetic moments. Knight shift data therefore indicate a rapid development of an impurity band below about 0.5 at. %. Spin-echo experiments show the presence of a second distorted gallium site in non-stoichiometric samples containing up to 1.0 at. % excess oxygen, the limit of the range studied. The fraction of substitutional sites decreases with increasing oxygen

content as does the carrier concentration at these sites. Knight shifts and spin-lattice relaxation rates remain correlated by the Korringa relation for the substitutional sites. Relaxation studies reveal that the distorted site is essentially decoupled from the conduction electrons. These results imply that the distorted sites are part of a diamagnetic carrier trap involving gallium complexed with a defect. We suggest that the complex consists of two gallium ions and an oxygen interstitial, i.e.  $\text{Ga}_2^{3+}\text{O}_i^{2-}$ .

Additionally, we report  $^{51}\text{V}$  and  $^{31}\text{P}$  NMR experiments in the series  $\text{ZrP}_{2-x}\text{V}_x\text{O}_7$  for  $x=2.0, 1.6, 1.0, 0.3$ , and  $0.0$ . Analysis of the  $^{51}\text{V}$  and  $^{31}\text{P}$  spectra for  $\text{ZrV}_2\text{O}_7$  and  $\text{ZrP}_2\text{O}_7$  show complex patterns consistent with the proposed  $P\bar{a}3$  space group and the  $3\times 3\times 3$  superstructure in which there exist 11 crystallographic distinct sites for phosphorous.  $^{51}\text{V}$  variable temperature MAS NMR in  $\text{ZrV}_2\text{O}_7$  exhibits evidence of the  $3\times 3\times 3$  superstructure at room temperature and shows that the ideal structure is reached by  $130^\circ\text{C}$ . The  $^{31}\text{P}$  spectrum in  $\text{ZrVPO}_7$  shows no evidence of superstructure.

NMR Study of Novel Oxides

by

Neil Roberts

A THESIS

submitted to

Oregon State University

in partial fulfillment of  
the requirements for the  
degree of

Doctor of Philosophy

Presented December 3, 2004

Commencement June 2005

Doctor of Philosophy thesis of Neil Roberts presented on December 3, 2004.

APPROVED:

**Redacted for Privacy**

\_\_\_\_\_  
Major Professor, representing Physics

**Redacted for Privacy**

\_\_\_\_\_  
Chair of the Department of Physics

**Redacted for Privacy**

\_\_\_\_\_  
Dean of Graduate School

I understand that my thesis will become part of the permanent collection of Oregon State University libraries. My signature below authorizes release of my thesis to any reader upon request.

Redacted for privacy

\_\_\_\_\_  
Neil Roberts, Author

## TABLE OF CONTENTS

	<u>PAGE</u>
1 Introduction.....	1
2 Overview of solid state NMR .....	2
2.1    The Zeeman Hamiltonian.....	2
2.2    Electron-Nuclear Interactions.....	3
2.2.1    Quadrupole Interactions.....	4
2.2.1.1    The Hamiltonian.....	4
2.2.1.2    The Energy Levels.....	7
2.2.2    Magnetic Interactions.....	8
2.2.2.1    The Chemical Shift.....	8
2.2.2.2    The Knight Shift.....	10
2.3    Spin-Lattice Relaxation.....	12
2.3.1    The Korringa Relation.....	12
2.4    Powder Patterns .....	13
2.5    Rate Equations.....	14
2.6    Experimental Considerations.....	17
2.6.1    The Spectrometer.....	17
2.6.1.1    Quadrature Detection.....	19
2.6.1.2    Variable Temperature Operation.....	23
2.6.1.3    Solid-Echo Pulse Sequence .....	23
2.6.1.4    The Probe Circuit .....	24
2.6.1.5    Magic Angle Spinning.....	25
3 Nuclear magnetic resonance investigation of the structure of phase transitions in the ZrV <sub>2-x</sub> P <sub>x</sub> O <sub>7</sub> Series .....	27
3.1    Introduction .....	27
3.2    Experimental Techniques.....	28
3.2.1    Samples .....	28

TABLE OF CONTENTS (Continued)		<u>PAGE</u>
3.2.2	NMR Techniques .....	28
3.3	Experimental Results .....	29
3.4	Conclusions .....	35
4	<sup>27</sup> Al and <sup>69</sup> Ga impurity nuclear magnetic resonance in ZnO:Al and ZnO:Ga .....	36
4.1	Introduction .....	36
4.2	Experimental Techniques .....	36
4.2.1	Sample Preparation and Characterization .....	36
4.2.1.1	Summary of Bulk Transport Properties .....	38
4.2.2	NMR Techniques .....	39
4.3	Experimental Results .....	40
4.3.1	Interpretation of Spectra .....	41
4.3.2	Resonance shifts .....	47
4.3.3	Spin-Lattice Relaxation .....	50
4.3.4	Zn <sub>0.98</sub> Ga <sub>0.02</sub> O <sub>1+z</sub> Series .....	55
4.4	Analysis and Interpretation .....	61
4.4.1	Zn <sub>1-x</sub> Ga <sub>x</sub> O .....	61
4.4.1.1	The Korringa Ratio .....	61
4.4.1.2	The Knight Shift .....	67
4.4.1.3	The Hyperfine Coupling $\langle  \psi_s(0) ^2 \rangle_{FS}$ .....	68
4.4.2	Zn <sub>0.98</sub> Ga <sub>0.02</sub> O <sub>1+z</sub> .....	69
4.5	Conclusions .....	72

FIGURE

## LIST OF FIGURES

PAGE

2-1: Basic schematic of an NMR spectrometer.....	17
2-2: Quadrature detection of the NMR signal. The NMR signal is split in two. One part is mixed with the reference signal in the lower PSD (phase sensitive detector), and one part is mixed with the reference signal shifted by 90° in a second PSD. The output of the PSD's goes the ADC's.....	21
2-3: a) Magnetization processing clockwise in the x-y plane of the coil, and the associated FID. b) Magnetization processing counter-clockwise and the associated FID. The FID's in a) and b) are the same. ....	22
2-4: Quadrupole echo pulse sequence.....	24
2-5: Details of NMR probe circuit. ....	25
3-1: Ideal structure for cubic $A^{4+}M_2^{5+}O_7$ compounds.....	27
3-2: $^{31}P$ NMR MAS spectrum for $ZrP_2O_7$ at room temperature. The broken line represents the model of 11 mostly Lorentzian peaks and 1 Gaussian peak at 46 ppm. The MAS frequency was 18 kHz, and the chemical shift reference was phosphoric acid. ....	29
3-3: $^{31}P$ NMR spectrum for $ZrVPO_7$ at room temperature.....	32
3-4: $^{51}V$ NMR spectra at various temperatures.....	34
4-1: Zn spectra in pure zinc oxide, sample Ga(0.03), and sample Ga(2), in a magnetic field of 8 Tesla. The spectrum for pure zinc oxide represents an axial quadrupole powder pattern.....	41
4-2: $^{69}Ga$ spectra in gallium doped zinc oxide at various concentrations in a magnetic field of 5.5 Tesla. ....	43
4-3: Comparison of spectra between both gallium isotopes at 5.5T and 8T at low and high dopant concentrations. The number to the right of each spectra is the FWHM in kHz.....	45
4-4: Comparison of time-domain spin-echoes between both gallium isotopes at 5.5T and 8T at low and high dopant concentrations. ....	46
4-5: Resonance shift vs. dopant concentration of $^{69}Ga$ in sample series Ga(x).....	47

<u>FIGURE</u>	<u>LIST OF FIGURES (Continued)</u>	<u>PAGE</u>
4-6:	Frequency shift vs. dopant concentration of $^{27}\text{Al}$ for sample series $\text{Al}(x)$ .....	48
4-7:	Frequency shift of Zn vs. dopant concentration in samples pure ZnO, Ga(0.03), and Ga(2).....	49
4-8:	$^{69}\text{Ga}$ spin-lattice relaxation rate vs. impurity concentration in sample series Ga(x).....	51
4-9:	$^{27}\text{Al}$ spin-lattice relaxation rate vs. impurity concentration in sample series Al(x). .....	52
4-10:	$^{69}\text{Ga}$ spin-lattice relaxation rate vs. temperature in samples Ga(3), Ga(2), and Ga(1). .....	53
4-11:	$^{27}\text{Al}$ spin-lattice relaxation rate vs. temperature for sample Al(2).....	54
4-12:	$^{69}\text{Ga}$ time domain spin-echoes vs. z in atomic percent. The oxygen pressure decreases from left to right and top to bottom. ....	56
4-13:	$^{69}\text{Ga}$ time domain spin-echo for sample Ga(2) ( $\text{Zn}_{0.98}\text{Ga}_{0.02}\text{O}:z = 0$ ). ....	56
4-14:	Shift of $^{69}\text{Ga}$ vs. z for sample series Ga(2)O(z). Included for comparison is the shift for sample Ga(2) (nominally $z = 0$ ). ....	58
4-15:	$^{69}\text{Ga}$ spin-lattice relaxation rate vs. z. ....	59
4-16:	Spectrum of $^{71}\text{Ga}$ in sample Ga(2)O(1).....	60
4-17:	Integrated intensity of the individual peaks 1 and 2 vs. relaxation time t, for sample Ga(2)O(1). Peak 1 is the site observed in series Ga(x). ....	60
4-18:	Square-root of the background-corrected spin-lattice relaxation rates versus total shift for $^{69}\text{Ga}$ in sample series Ga(x) (solid circles) and series Ga(2)O(z) (open circles). Solid line represents linear least squares fit to the series Ga(x) and the dashed line is drawn with slope given by the Korringa Relation, for $^{27}\text{Al}$ . ....	64
4-19:	$^{69}\text{Ga}$ Knight shift, corrected for chemical shift, versus nominal gallium concentration x for the stoichiometric series Ga(x). Dashed line represents nearly-free-electron behavior $K \propto x^{1/3}$ .....	65

FIGURE

LIST OF FIGURES (Continued)

PAGE

- 4-20: In the graph  $\left(\frac{1}{T_1}\right)_{Korringa}$  in the relaxation rate calculated from the measured Knight shifts and  $\left(\frac{1}{T_1}\right)_{magnetic}$  is the measured relaxation rate corrected for a quadrupolar contribution. .... 66
- 4-21: The Korringa ratio vs. impurity concentration for the series Ga(x). The error bars are relative. The absolute uncertainty is about  $\pm 15\%$ . The line represents a fit to a constant and has the value 0.92..... 67
- 4-22:  $^{69}\text{Ga}$  Knight shift of nonstoichiometric samples  $\text{Zn}_{0.98}\text{Ga}_{0.02}\text{O}_{1+z}$ , corrected for chemical shift, versus substitutional gallium content  $x_s$  determined from spin-echo shapes. Dashed line represents nearly-free-electron behavior,  $K \propto x_s^{1/3}$ . The corrected Knight shift value of the broad line component is also shown (open square)..... 71

<u>TABLE</u>	<u>LIST OF TABLES</u>	<u>PAGE</u>
Table 3-1:	$^{31}\text{P}$ Parameters for the series $\text{ZrV}_{2-x}\text{P}_x\text{O}_7$ .....	31
Table 4-1:	List of samples and associated impurity concentration.....	38
Table 4-2:	Properties of NMR isotopes.....	40

## 1 INTRODUCTION

Over one hundred nuclear isotopes exist in nature with non-zero magnetic moments. Nuclear Magnetic Resonance (NMR) is the experimental technique in which these magnetic moments are used as probes to explore the structure and dynamics of materials. The fact that many nuclei are NMR accessible is a key advantage, making many if not most materials experimental candidates. Consequently, NMR has permeated nearly all fields of material science involving a vast range of applications. Its widespread use has been the impetus for development of the technique over the past 50 years.

Additionally, NMR is a very local and non-intrusive probe, yielding information about the fields interacting at the nuclear site. This local nature is often complementary to mesoscopic and bulk methods.

Although nature provides a plethora of isotopes, many exist in low abundance or with small magnetic moments, providing only a weak NMR signal, challenging the experimentalist.

In this work NMR is used to study inorganic oxides in the solid state.

One such class of materials is impurity doped ZnO. The dopants are the Group III elements Al and Ga, and the resultant material is a heavily doped n-type semiconductor. This material is of interest as a transparent electrical conductor. It has the advantage of being low cost and non-toxic. Applications range from additives to polymers and paper to prevent static electricity buildup, to optical displays.

Another class of materials studied in this work is characterized by the ability to show strong isotropic negative thermal expansion. Our goal here is to use NMR to assist with the understanding of the structure and thermal mechanisms in these materials.

## 2 OVERVIEW OF SOLID STATE NMR

The system of interest in an NMR experiment is a collection of nuclei with magnetic dipole moments. A static magnetic field is then applied to the system to prepare it in an equilibrium state of net magnetization (given by Curie's law), which is the net sum of the individual nuclear moments. The individual moments precess about their local magnetic field. However, the applied static field also interacts (in general) with the environment (specifically the lattice) for which the system is coupled. For instance in solids, orbital motion of bonding electrons is induced, creating a contribution to the local field in addition to the static field. Other examples are the spin polarizations of conduction electrons and magnetic defects. These additional contributions to the local field at the nuclear site are called "hyperfine fields".

Fluctuations in the hyperfine field provide a mechanism for energy transfer to/from the nuclear spins and the lattice. This causes the spins to eventually equilibrate with the static magnetic field. This process is called spin-lattice relaxation.

NMR provides a means to experimentally investigate hyperfine fields and the associated dynamics of spin-lattice relaxation which yields detailed information about the local environment of the probe nuclei.

### 2.1 The Zeeman Hamiltonian

The interaction energy of a nucleus in a static magnetic field is described by the Zeeman Hamiltonian,

$$H_{zeeman} = -\vec{\mu} \cdot \vec{H}, \quad (2.1)$$

where  $\vec{H}$  is the external magnetic field and  $\vec{\mu}$  is the nuclear magnetic moment. The nuclear magnetic moment is proportional to the spin angular momentum  $\vec{J}$  of the nucleus and can be written,

$$\vec{\mu} = \gamma \hbar \vec{I}, \quad (2.2)$$

where  $\gamma$  is the nuclear gyromagnetic ratio,  $\hbar$  is Planck's constant, and

$$\vec{J} = \hbar \vec{I} . \quad (2.3)$$

$\vec{I}$  is therefore dimensionless. If the external field is in the z-direction,

$$\vec{H} = H_0 \hat{k} , \quad (2.4)$$

the Hamiltonian becomes,

$$H_{zeeman} = \gamma \hbar H_0 I_z . \quad (2.5)$$

The spin state of the nucleus is specified by the quantum numbers  $I$  and  $m$  where  $I$  is the total spin and  $m$  is the z-component. The application of a static magnetic field results in a splitting of the  $2I+1$  degenerate states. The difference in energy of any two adjacent levels is  $\gamma \hbar H_0$ .

## 2.2 Electron-Nuclear Interactions

The usefulness of NMR arises from the fact that the nucleus is in general not isolated in the external magnetic field. In an atom, for example, the nucleus will interact with the internal fields produced by electrons of the atom. In a crystal lattice the nucleus will interact with other nuclei, the crystal field, and possibly conduction electrons and impurities and defects. The effect of such fields is a perturbation of the Zeeman energy levels and a source of relaxation. They are manifest in the structure of the absorption spectrum and in the spin dynamics. This section is concerned with the effect on the Zeeman levels resulting from the interaction of the nucleus with electrons. In a solid the electrons can reside in closed shells about the nucleus, participate in bonding, be itinerant, as in a metal, or localized in the vicinity of the nucleus are some possibilities. The electrons in the system will of course interact with the external magnetic field. Therefore, the electron-nuclear interaction is a simultaneous interaction between the electrons and the static external field and the electrons and the nucleus. Additionally, for quadrupolar nuclei ( $\text{spin} > 1/2$ ), the quadrupole moment of the nucleus will interact with the electric field gradient of the crystal lattice. This interaction partially lifts the degeneracy of the nuclear spin energy levels at zero applied magnetic field, and shifts the levels in a non-zero applied magnetic field.

## 2.2.1 Quadrupole Interactions

In addition to magnetic interactions the electric quadrupole moment of a nucleus will interact with the electric field gradient of the electronic charge distribution. In this section the nuclear electric quadrupole Hamiltonian and its effect on the Zeeman energy levels will be reviewed. P.P. Man<sup>1</sup> supplies a good comprehensive review of this subject.

### 2.2.1.1 The Hamiltonian

Classically, the interaction energy of a charge density  $\rho(\vec{r})$  with an external potential  $V(\vec{r})$  is

$$E = \int \rho(\vec{r})V(\vec{r})d\tau . \quad (2.6)$$

In our problem  $\rho(r)$  is the nuclear charge density and  $V(\vec{r})$  is the potential due to charges external to the nucleus.  $d\tau$  is a differential volume element. Expanding about  $r = 0$ , the nuclear site, we obtain,

$$E = V(0) \int \rho(\vec{r})d\tau + \sum_{\alpha} V_{\alpha} \int x_{\alpha} \rho(\vec{r})d\tau + \frac{1}{2!} \sum_{\alpha, \beta} V_{\alpha\beta} \int x_{\alpha} x_{\beta} \rho(\vec{r})d\tau + \dots \quad (2.7)$$

In this expression,

$$V_{\alpha} = \left. \frac{dV}{dx_{\alpha}} \right|_{r=0} \quad (2.8)$$

and,

$$V_{\alpha\beta} = \left. \frac{d^2V}{dx_{\alpha} dx_{\beta}} \right|_{r=0} , \quad (2.9)$$

where  $\alpha, \beta = 1, 2, 3$ , so that  $x_1, x_2, x_3 = x, y, z$ .

The zeroth order term is simply the electrostatic energy of a point charge. The first order term is zero because nucleons have zero electric dipole moment. The reason for this is that nucleons have definite parity and the center of mass is coincident with the center of charge. The second order term is the electric quadrupole term. The third order term (not shown) vanishes for the same reason as the first order term. The

fourth order term, or hexadecapole term, is  $10^{-8}$  times smaller than the quadrupole term. We consider only the quadrupole term.

$V_{\alpha\beta}$  is called the electric field gradient tensor (EFG). It is a second rank symmetrical tensor. First we note that we can always find a principal axis system (PAS) such that,  $V_{\alpha\beta} = 0$  for  $\alpha \neq \beta$ . Additionally, using Laplace's equation,  $\vec{\nabla}^2 V = 0$ , since we consider the field gradient arising from sources external to the nucleus and therefore,  $\sum_{\alpha} V_{\alpha\alpha} = 0$  at the nucleus. The EFG is traceless.

We now define the traceless tensor (motivation to become apparent),

$$Q_{\alpha\beta} = \int (3x_{\alpha}x_{\beta} - \delta_{\alpha\beta}r^2)\rho(\vec{r})d\tau. \quad (2.10)$$

With this definition the interaction energy can be written,

$$E = \frac{1}{6} \sum_{\alpha,\beta} (V_{\alpha\beta}Q_{\alpha\beta} + V_{\alpha\beta}\delta_{\alpha\beta} \int r^2 \rho(\vec{r})d\tau). \quad (2.11)$$

The second term is independent of nuclear orientation and is therefore dropped so that,

$$E = \frac{1}{6} \sum_{\alpha,\beta} V_{\alpha\beta}Q_{\alpha\beta}. \quad (2.12)$$

We now apply the correspondence principle to the charge density of the nucleus,

$$\rho^{(op)}(\vec{r}) = e \sum_{\text{protons}} \delta(\vec{r} - \vec{r}_k), \quad (2.13)$$

so that the nuclear quadrupole Hamiltonian becomes,

$$H_Q = \frac{1}{6} \sum_{\alpha,\beta} V_{\alpha\beta}Q_{\alpha\beta}^{(op)}. \quad (2.14)$$

Note that the electric field gradient is treated classically whereas  $Q_{\alpha\beta}$  is a quantum mechanical operator. Also, we do not consider excited states of the nucleus for these are expected to be far away in energy.

The Wigner-Eckart Theorem states all traceless, second rank, symmetric

tensors are proportional so that,

$$(Im|Q_{\alpha\beta}|Im') = C(Im|\frac{3}{2}(I_{\alpha}I_{\beta} + I_{\beta}I_{\alpha}) - \delta_{\alpha\beta}I^2|Im'). \quad (2.15)$$

The constant C is defined such that,

$$eQ = (II|Q_{zz}|II) = C(II|3I_z^2 - I^2|II) = CI(2I - 1), \quad (2.16)$$

where Q is termed the quadrupole coupling constant. The Hamiltonian is then written,

$$H_Q = \frac{eQ}{6I(2I-1)} \sum_{\alpha,\beta} V_{\alpha\beta} [\frac{3}{2}(I_{\alpha}I_{\beta} + I_{\beta}I_{\alpha}) - \delta_{\alpha\beta}I^2], \quad (2.17)$$

or,

$$H_Q = \frac{eQ}{4I(2I-1)} [V_0(3I_z^2 - I^2) + V_{+1}(I^-I_z + I_zI^-) + V_{-1}(I^+I_z + I_zI^+) + V_{+2}(I^-)^2 + V_{-2}(I^+)^2], \quad (2.18)$$

where,

$$\begin{aligned} V_0 &= V_{zz} \\ V_{\pm 1} &= V_{zx} \pm iV_{zy} \\ V_{\pm 2} &= \frac{1}{2}(V_{xx} - V_{yy}) \pm iV_{xy} \end{aligned} \quad (2.19)$$

Also, it is convenient to write  $H_Q$  in the principal axis system (PAS),

$$H_Q^{PAS} = \frac{e^2Qq}{6I(2I-1)} [3I_z^2 - I(I+1) + \frac{1}{2}\eta(I_+^2 + I_-^2)], \quad (2.20)$$

where,

$$\begin{aligned} eq &= V_{zz} \\ \eta &= \frac{V_{xx} - V_{yy}}{V_{zz}}, \end{aligned} \quad (2.21)$$

$\eta$  is called the asymmetry parameter.  $\eta$  is nonzero for symmetries lower than axial.

For example,

$$\begin{aligned}
\text{Cubic Symmetry} &\longrightarrow V_{xx} = V_{yy} = V_{zz} \\
\text{Axial Symmetry} &\longrightarrow V_{xx} = V_{yy}; \sum_{\alpha} V_{\alpha\alpha} = 0
\end{aligned} \tag{2.22}$$

### 2.2.1.2 The Energy Levels

Assuming  $H_Q \ll H_{zeeman}$ , which is often the case in NMR, the shift of the Zeeman energy levels, and therefore the transition frequencies  $\nu(m \longleftrightarrow m-1)$ , can be calculated using stationary perturbation theory. The result is,

$$\nu(m \longleftrightarrow m-1) = \nu_0 + \nu^1 + \nu^2, \tag{2.23}$$

where  $\nu_0$  is the Larmor frequency, and  $\nu^1$ , and  $\nu^2$  are the first and second order frequency shifts respectively. These are given by,

$$\nu^1 = \frac{1}{2} \nu_Q (m - \frac{1}{2})(3 \cos^2 \theta - 1) - \frac{1}{2} (m - \frac{1}{2}) \nu_Q \eta \sin^2 \theta \cos 2\phi, \tag{2.24}$$

and,

$$\nu_{central}^2 = -\frac{\nu_Q^2}{\nu_0} (I(I+1) - \frac{3}{4}) [A(\phi, \eta) \cos^4 \theta + B(\phi, \eta) \cos^2 \theta + C(\phi, \eta)], \tag{2.25}$$

where  $\nu_{central}$  indicates the frequency shift of the central transition ( $\frac{1}{2} \longrightarrow \frac{-1}{2}$ ). In

the above expressions  $\nu_Q$  is the quadrupole frequency parameter,

$$\nu_Q = \frac{3e^2qQ}{2I(2I-1)} V_{zz}, \tag{2.26}$$

and  $\theta$  and  $\phi$  are the polar and azimuthal angles respectively which describe the orientation of the principal axis with respect to the external applied magnetic field, and

$$\begin{aligned}
A(\alpha, \eta) &= -\frac{27}{8} + \frac{9}{4} \eta \cos 2\alpha - \frac{3}{8} (\eta \cos 2\alpha)^2, \\
B(\alpha, \eta) &= \frac{30}{8} - \frac{1}{2} \eta^2 - 2\eta \cos 2\alpha + \frac{3}{4} (\eta \cos 2\alpha)^2, \\
C(\alpha, \eta) &= -\frac{3}{8} + \frac{1}{3} \eta^2 - \frac{1}{4} \eta \cos 2\alpha - \frac{3}{8} (\eta \cos 2\alpha)^2.
\end{aligned} \tag{2.27}$$

In second order only the frequency shift of the central transition is given although a more general expression for any transition exists<sup>2</sup>.

Several comments are in order. To first order the central transition is unaffected, however, the satellites will have an anisotropic shift (i.e. the shift depends on the orientation of the crystal axis). In second order the central transition is shifted anisotropically, and the satellites are shifted additionally. However, their pair-wise separation remains the same as in first order.

## 2.2.2 Magnetic Interactions

### 2.2.2.1 The Chemical Shift

The effect on the Zeeman energy levels due to filled electronic orbits is called the chemical shift. The shift is sensitive to the electronic structure of the closed shells and is therefore an important parameter measured with NMR. Chemical shifts are proportional to the applied field, and the field at the nucleus is written,

$$H_{nucleus} = (1 + \tilde{\sigma}) \cdot \vec{H}_0, \quad (2.28)$$

where  $\tilde{\sigma}$  is the chemical shift usually reported in parts per million (ppm).  $\tilde{\sigma}$  is a tensor quantity with anisotropy arising from dependence on the orientation of the principal axis with respect to the applied field.  $\tilde{\sigma}$  has contributions from a diamagnetic term (resulting from fields induced antiparallel to the applied field) and a paramagnetic term (resulting from fields induced parallel to the applied field),

$$\tilde{\sigma} = \tilde{\sigma}_D + \tilde{\sigma}_p. \quad (2.29)$$

$\tilde{\sigma}_D$  represents the coupling between the nuclear moments and the magnetic field of the currents induced by the Larmor precession of the electrons in the applied field.

The Hamiltonian for this interaction is,

$$H_D = \frac{\gamma \hbar e^2}{2mc} \sum_{k^n} \frac{(\vec{H}_0 \times \vec{r}_k) \cdot (\vec{I} \times \vec{r}_k)}{r_k^3}, \quad (2.30)$$

where  $\vec{r}_k$  is the position vector from the nucleus in question to the  $k^{\text{th}}$  electron, and the sum is over a total of  $n$  electrons. Using the first order change in the energy, the interaction can be written,

$$H_D = \gamma \hbar \vec{l} \cdot \tilde{\sigma}_D \cdot \vec{H}_0. \quad (2.31)$$

$$\tilde{\sigma}_D = \underbrace{\sigma_D}_{\text{isotropic}} + \underbrace{\tilde{\sigma}'_D}_{\text{anisotropic}}$$

The tensor,  $\sigma_D$ , can be decomposed into the sum of a scalar part and a traceless part. The prime indicates a traceless tensor. As labeled in the equation the traceless part results in an anisotropy in the interaction. The paramagnetic shift  $\tilde{\sigma}_p$  results from considering interactions to second order. The Hamiltonian for this case is,

$$H_p = \sum_k H^{\text{ZL}} \cdot C \cdot H_k^{\text{SO}}, \quad (2.32)$$

where,

$$C = \sum \frac{|n\rangle\langle n|}{E_0 - E_n}, \quad (2.33)$$

and  $H^{\text{ZL}}$ , and  $H_k^{\text{SO}}$ , represent the orbital Zeeman energy of the electrons and the spin orbit coupling of the nucleus with the  $k^{\text{th}}$  electron respectively. It is seen that the paramagnetic shift depends on the mixing of excited states with the ground state. It is in essence an unquenching of the orbital momentum (see section 2.2.2.2) in the presence of the static field  $H_0$ .

In complete analogy with  $\tilde{\sigma}_D$ , one can write,

$$H_p = \gamma \hbar \vec{l} \cdot \tilde{\sigma}_p \cdot \vec{H}_0, \quad (2.34)$$

$$\tilde{\sigma}_p = \underbrace{\sigma_p}_{\text{isotropic}} + \underbrace{\tilde{\sigma}'_p}_{\text{anisotropic}}$$

where  $\tilde{\sigma}_p$  is the sum of a scalar and traceless part.

Taking this opportunity to define some notation we note that what is measured is the total chemical shift ( i.e. the sum of the diamagnetic and paramagnetic contributions) so that,

$$\tilde{\sigma} = \tilde{\sigma}_D + \tilde{\sigma}_P = \sigma_{iso} + \tilde{\sigma}'_{aniso}, \quad (2.35)$$

where,

$$\begin{aligned} \sigma_{iso} &= \sigma_D + \sigma_P \\ \tilde{\sigma}'_{aniso} &= \tilde{\sigma}'_D + \tilde{\sigma}'_P \end{aligned} \quad (2.36)$$

In summary,

$$\begin{aligned} H_{CS} &= H_D + H_P \\ &= \gamma \hbar \sigma_{iso} \vec{I} \cdot \vec{H}_0 + \gamma \hbar \vec{I} \cdot \tilde{\sigma}'_{aniso} \cdot \vec{H}_0 \end{aligned} \quad (2.37)$$

For example, in the case of cubic symmetry, there is only  $\sigma_{iso}$ , and the resonant frequency is given by,

$$\nu = \nu_0 + \sigma_{iso} \nu_0. \quad (2.38)$$

In practice, a reference sample with frequency  $\nu_{ref}$  is chosen such that  $\nu_{ref} \cong \nu_0$ . The chemical shift can then be measured according to,

$$\sigma_{iso} = \frac{\nu - \nu_{ref}}{\nu_{ref}} \quad (2.39)$$

In cases of lower symmetry,  $\nu$  will depend on the orientation of the crystal axis with the applied magnetic field determined by  $\tilde{\sigma}'_{aniso}$ . In a single crystal,  $\tilde{\sigma}'_{aniso}$  can be determined by measuring  $\nu$  while varying the orientation of the crystal axis. In a powder sample, the anisotropy leads to a well defined spectral distribution (see section 2.4).

### 2.2.2.2 The Knight Shift<sup>3</sup>

The dipole moment of the nucleus will interact with the magnetic field of conduction electrons. The result is an effective field at the nucleus causing a shift in the resonant frequency, and this is called the Knight shift after its discoverer. As in the case of the chemical shift, the Knight shift is proportional to the applied field and is a tensor quantity. The field at the nucleus is then,

$$H_{nucleus} = (1 + \tilde{K}) \cdot \vec{H}_0 \quad (2.40)$$

The electron-nuclear Hamiltonian is,

$$H = 2 \frac{8\pi}{3} \mu_\beta \gamma_n \hbar \vec{I} \cdot \vec{S}(\vec{r}) \delta(\vec{r}) - 2 \mu_\beta \gamma_n \hbar \vec{I} \cdot \left[ \frac{\vec{S}}{r^3} - \frac{3\vec{r}\vec{S} \cdot \vec{r}}{r^5} \right] - \gamma_n \hbar \frac{e}{mc} \left[ \vec{I} \cdot \frac{\vec{L}}{r^3} \right], \quad (2.41)$$

where  $\mu_\beta$  is the Bohr magnetron,  $\vec{S}(\vec{r})$  is the electron spin angular momentum operator, and  $\vec{L}$  is the electron orbital angular momentum operator.

The first term is the contact interaction term and will contribute to the interaction energy only in the case where there exists overlap of the electronic wave function with the nucleus, that is, the wavefunction must contain at least some mixture of *s*-like symmetry. It can be shown<sup>3,4</sup> that this produces an isotropic shift in frequency given by,

$$\nu = \nu_0 + \nu_0 \frac{8\pi}{3} \chi_p \left\langle |\psi_s(0)|^2 \right\rangle_{FS} \quad (2.42)$$

where  $\chi_p$  is the Pauli paramagnetic spin susceptibility per atom, and  $\left\langle |\psi_s(0)|^2 \right\rangle_{FS}$  is the square of the *s*-wave function at the nucleus averaged over those electrons at the Fermi surface (FS). The isotropic Knight shift is then defined as,

$$K_{iso} = \frac{8\pi}{3} \chi_p \left\langle |\psi_s(0)|^2 \right\rangle_{FS} \quad (2.43)$$

The second term is the usual spin-dipolar term and gives contributions from states with lower than *s*-symmetry (i.e. *p*-states). This term contributes to an anisotropic shift in the same way as discussed in section 2.2.2.1 for the chemical shift, in cases of less than cubic symmetry. In general the total Knight shift can be parameterized,

$$K = K_{iso} + \frac{K_1}{2} \{ (3 \cos^2 \theta - 1) - \varepsilon \sin^2 \theta \cos 2\phi \}, \quad (2.44)$$

where,

$$K_1 = K_{aniso}(z) \quad (2.45)$$

and,

$$\varepsilon = \frac{K_{aniso}(y) - K_{aniso}(x)}{K_{aniso}(z)} \quad (2.46)$$

In the case of axial symmetry ( $\varepsilon = 0$ ),

$$\frac{K_1}{2} = K_{axial} = \chi_p \left\langle \int \psi^* (3z^2 - r^2) r^{-5} \psi dV \right\rangle_{FS} (3 \cos^2 \theta - 1). \quad (2.47)$$

Finally, the third term is the interaction of the nuclear spin with the orbital motion of the electrons. In diamagnetic substances and most metals the orbital momentum is quenched, meaning  $\langle 0 | \vec{L} | 0 \rangle = 0$ , where  $\langle 0 |$  is the ground state. This effect arises whenever the crystalline electric fields leave a state nondegenerate, for in this case the eigenfunction is real. Therefore, the matrix element either vanishes or is pure imaginary, but the diagonal matrix element of a Hermitian operator is always real, and so the matrix element must vanish.

## 2.3 Spin-Lattice Relaxation

### 2.3.1 The Korringa Relation

In the case of a simple metal the response of the nuclear spin system is dominated by its interaction with s-electron spins through the Fermi contact interaction (see eqn. 2.42),

$$H_{contact} = 2 \frac{8\pi}{3} \mu_\beta \gamma_n \hbar \vec{I} \cdot \vec{S} \delta(\vec{r}). \quad (2.48)$$

As discussed in section 2.2.2.2, the interaction is the source of the Knight shift,

$$K_{iso} = \frac{8\pi}{3} \chi_p \left\langle |\psi_s(0)|^2 \right\rangle_{FS}. \quad (2.49)$$

Four experimental observations characterize the Knight shift. 1)  $K$  is positive, 2)  $K$  is independent of the applied field, 3)  $K$  is nearly independent of temperature, and 4)  $K$  increases in general with increasing nuclear charge  $Z$ .

The contribution to the spin-lattice relaxation rate,  $1/T_1$ , from s-electrons through the Fermi contact interaction is given by,

$$\frac{1}{T_1} = \frac{64}{9} \pi^3 \hbar^3 \gamma_e^2 \gamma_n^2 \left\langle |\psi_s(0)|^2 \right\rangle_{FS} \rho^2(E_F) kT, \quad (2.50)$$

where  $\rho(E_F)$  is the electron density of states at the Fermi level,  $k$  is Boltzman's factor, and  $T$  is the absolute temperature. Comparing this result to that of the Knight shift with  $\chi_p$ , gives the Korringa relation<sup>5</sup>,

$$\left( \frac{1}{T_1} \right)_{Korringa} = \frac{4\pi kT}{\hbar} \frac{\gamma_n^2}{\gamma_e^2} K^2. \quad (2.51)$$

The Korringa ratio is then defined as

$$\eta = \frac{\left( \frac{1}{T_1} \right)_{Measured}}{\left( \frac{1}{T_1} \right)_{Korringa}}, \quad (2.52)$$

where  $\left( \frac{1}{T_1} \right)_{Korringa}$  is calculated from the measured Knight shift.  $\eta$  is a measure of the deviation from ideal metallic behavior.  $\eta = 1$  denotes a perfect metal.

## 2.4 Powder Patterns

It was shown previously that quadrupolar and magnetic interactions are in general anisotropic, meaning that the resonance frequency is a function of the orientation of the crystal axis with the applied field. In a single crystal, therefore, the line position will shift as the sample is rotated.

However, a powder consists of an ensemble of crystallites and a distribution of orientations. The resulting spectrum is called the normalized shape function or a powder pattern. Powder patterns can be represented by the following equation,

$$g(\nu) = \int \Omega P(\Omega) \delta(\nu - \nu(\theta, \phi)) d\Omega, \quad (2.53)$$

where  $g(\nu)$  is the powder pattern,  $P(\Omega)$  is the probability that the principal axis of a given crystallite has the orientation with respect to the applied field described by the solid angle  $\Omega$ .  $\nu(\theta, \phi)$  is the orientation dependent frequency resulting from anisotropy in the hyperfine interactions.

If the laboratory field exerts no torques on the crystallites they will be oriented at random and therefore,

$$P(\Omega) = \frac{1}{4\pi}, \quad (2.54)$$

giving,

$$g(\nu) = \int_0^\pi d\theta \int_0^{2\pi} d\phi \delta(\nu - \nu(\theta, \phi) \sin \theta). \quad (2.55)$$

For simple cases involving axial symmetry the powder pattern can be calculated analytically. In general a numerical solution is necessary, and in fact is quite simple.

## 2.5 Rate Equations

The general procedure for measuring the spin-lattice relaxation rate,  $1/T_1$ , is to prepare the spin system in a state of non-equilibrium and then to observe the longitudinal magnetization as a function of time. The question then becomes what is the proper way to extract  $T_1$  from such data. The general solution is to "fit" the data to the expected magnetization recovery curve of which  $T_1$  is a parameter. Magnetization recovery curves are calculated in the literature and hence only an outline of the salient features will be given.

The form of the magnetization recovery curve depends on the spin, the static splitting of the energy levels, and the nature of the interaction responsible for relaxation (i.e. magnetic or quadrupolar). It does not depend on the details of the system or interaction such as temperature dependence or field dependence. These details are manifest in the parameter  $T_1$ . The character of the relaxation is a result of the fact that the polarizations of the various transitions are interdependent leading to set of coupled rate equations for the time dependence of the polarizations.

First define,

$$n_m(t) = N_m(t) - N_{m0}, \quad (2.56)$$

as the difference in the population of level  $m$  away from equilibrium, and,

$$a_m(t) = n_m(t) - n_{m-1}(t), \quad (2.57)$$

which is proportional to the magnetization. Then,

$$\frac{da_m(t)}{dt} = \sum_{m'} W_{mm'} a_{m'}(t), \quad (2.58)$$

where  $m'$  runs over  $2I$  values, and the  $W_{mm'}$  depend on the transitions allowed by the relaxation mechanism and the rates of these transitions.

The general solution becomes,

$$a_m(t) = \sum_{m'} \alpha_{mm'} \exp(-W_{m'} t). \quad (2.59)$$

The constants  $\alpha_{mm'}$  depend on the initial conditions and  $W_m$  are the eigenvalues associated with the matrix defined by the  $W_{mm'}$ . If the source of relaxation is magnetic, selection rules dictate that only transitions between adjacent levels are allowed\* and the transition rate can be written,

$$W_{m\pm 1 \rightarrow m} = W(I \mp m)(I \pm m + 1). \quad (2.60)$$

This will be true, for example, when the source of relaxation is due to coupling to conduction electrons in a metal or coupling to spin diffusion resulting from the existence of a paramagnetic impurity. The latter is often the main source of relaxation in insulating solids where the NMR nuclei has spin  $\frac{1}{2}$  and does not couple to phonons. Now is considered two special cases for magnetic interactions.

First, for the case  $I=I/2$ , equation (2.60) gives,

$$\alpha_{1/2}(t) \propto M(t) - M_{eq} = \alpha_{1/2} \exp(-2Wt), \quad (2.61)$$

and,

$$\alpha_{1/2} = M(0) - M_{eq}, \quad (2.62)$$

where  $M_{eq}$  is the equilibrium magnetization and  $M(0)$  is the initial magnetization.

Rearranging,

$$M(t) = (M(0) - M_{eq}) \exp(-t/T_1) + M_{eq}. \quad (2.63)$$

---

\* Another example is the case where the relaxation mechanism is quadrupolar. In this case equation (2.18) dictates the following selection rules  $\Delta m = \pm 1, \pm 2$ .

Therefore in the absence of sample inhomogeneity or inequivalent nuclear sites a spin  $\frac{1}{2}$  nuclei will exhibit single exponential spin-lattice relaxation. Phosphorous is an example of a spin  $\frac{1}{2}$  nuclei studied in the following chapter.

Secondly, and with greater consequence,  $I > 1/2$  is considered. Examples of quadrupolar nuclei studied in the following chapters are vanadium ( $7/2$ ), zinc ( $5/2$ ), aluminum ( $5/2$ ), and gallium ( $3/2$ ). For half-integer nuclei, in an environment of lower than cubic symmetry, the satellite transitions are often split from the central transition to such a degree that application of an rf-pulse at the central transition frequency leaves other energy levels unperturbed. In this case only the central transition is usually observed. The following equations are examples of magnetization recovery curves for this situation where magnetic relaxation is assumed.

$$M(t) = (M(0) - M_{eq})[0.1 \exp(-t/T_1) + 0.9 \exp(-6t/T_1)] + M_{eq}, \quad (2.64)$$

for  $I=3/2$ , and

$$M(t) = (M(0) - M_{eq})[0.03 \exp(-t/T_1) + 0.18 \exp(-6t/T_1) + 0.79 \exp(-15t/T_1) + M_{eq}] \quad (2.65)$$

for  $I=5/2$ .

## 2.6 Experimental Considerations

### 2.6.1 The Spectrometer

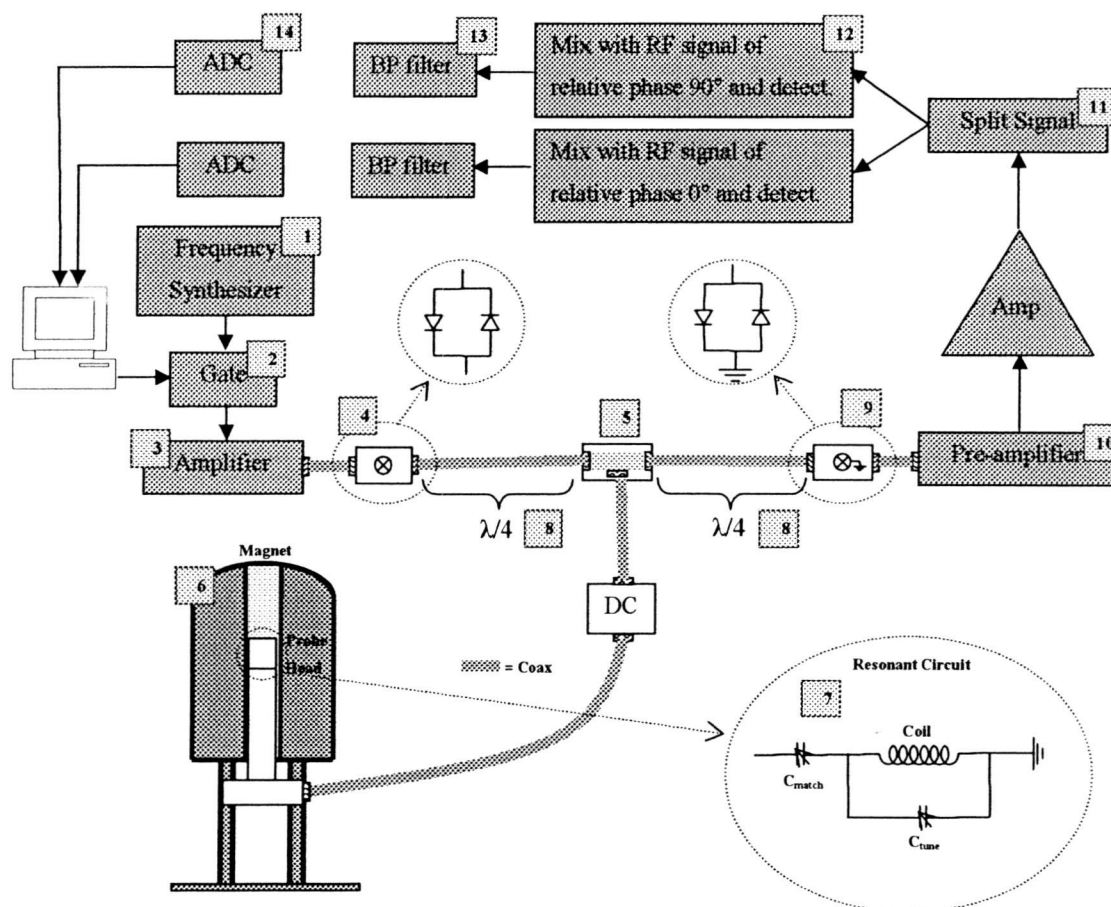


Figure 2-1: Basic schematic of an NMR spectrometer.

Figure 2-1 is a basic schematic of an NMR spectrometer. It is intended to expose only the critical hardware components and signal processing procedures. It represents a gross simplification of an actual spectrometer.

A radio frequency (RF) signal is generated in the synthesizer (1). Usually (although certainly not always), an RF pulse or pulse sequence is desired. The Gate (2) is used to create RF pulses with precise timing. Pulse widths are typically several microseconds to  $10^3$ 's of microseconds depending on the magnetic moment of the

probe nuclei and the magnitude of the RF field generated in the coil (i.e. the time for a  $90^\circ$  rotation of the magnetization is determined by  $\gamma H_1 t_{pw} = \pi/2$ , where  $\gamma$  is the gyromagnetic ratio and is proportional to the magnetic moment,  $H_1$  is the magnitude of the RF field, and  $t_{pw}$  is the duration of the pulse width). The pulse is then amplified (3) to a high power, typically 100's of watts and output to 50 $\Omega$  coaxial cable. The crossed-diode array (4) behaves as a voltage dependent switch. Closed for large voltages and is open for small voltages (turn on voltage  $\approx 0.5V$ ). Since the pulse is high power, the switch is closed. At the duplexer (5), the impedance seen at the port going to the pre-amplifier is large. This is because the quarter-wave transmission line (8) transforms the small impedance of the crossed-diodes connected to ground (9) according to<sup>6</sup>

$$Z_{in} = \frac{|Z_0|^2}{Z_{crossed-diodes}}, \quad (2.66)$$

where,  $Z_0$  is the 50 $\Omega$  characteristic impedance. The transmitted pulse is therefore directed to the other output port of the duplexer, ultimately going to the sample. The sample is contained in the coil of the resonant circuit (7). In a single coil design, the coil acts as both the mechanism for applying the RF magnetic field and the NMR signal detector. Following the RF pulse (or pulse sequence), the resulting NMR signal is detected in the coil. The NMR signal voltage produced by the coil is many orders of magnitude smaller than the applied pulse (typically  $\mu V$  to mV). This is well below the turn-on voltage of the crossed-diodes. The amplifier is now effectively isolated from the network. Also, the quarter-wave line transforms a now large impedance in the crossed-diodes to a small impedance at the duplex port going to the pre-amplifier (Note: the crossed-diodes (9) also provide input power protection to the pre-amplifier). The small NMR signal is then pre-amplified and subsequently amplified.

The NMR signal is then split in 2. Both signals are then mixed with the RF carrier frequency (the same RF as the pulse) retaining only the near DC components (The

fact that the carrier signals are  $90^\circ$  out of phase will be discussed subsequently). Band pass filters (13) are common to reduce noise, and then finally the analog signals are converted to digital (14).

### 2.6.1.1 Quadrature Detection

Quadrature detection (QD) was an important enabling technology for NMR spectroscopy (this is true in other fields as well an example being the detection of radar signals). For instance, it eliminates the need to adjust the phase of the detection circuitry to detect the maximum signal. Additionally, the sign of the position of a resonant signal (e.g. whether it is above or below the reference frequency) cannot be determined without adjusting experimental parameters or some kind of quadrature detection scheme. All modern spectrometers implement quadrature detection. In this section the basic idea of quadrature detection and its advantages are discussed.

The NMR signal results from the precession of the component of the net magnetization,  $\vec{M}$  in the plane of the pick up coil. This signal is radio frequency (In the absence of local hyperfine fields, the frequency is the Larmor frequency,  $\omega_L = -\gamma H_0$ ). Consider the situation, whereby using the appropriate RF pulse with a carrier frequency sufficiently close to that of the resonant frequency,  $\vec{M}$  is configured to lie in the x-direction, which at this instance in time coincides with the axis of the coil. The signal is then detected by the spectrometer by mixing with the carrier frequency<sup>7</sup>. The resulting base band signal is called the free induction decay or FID. The FID generally consists of a distribution of resonant frequencies. The resonant frequency's and the carrier frequency generally differ slightly creating an audio output which will decay over time due to a loss of phase coherence. The graphs in Figure 2-3 represent typical single frequency component FID's.

In a reference frame rotating at the carrier frequency, the magnetization will precess either clockwise or counterclockwise depending on whether the resonant frequency is above or below the carrier frequency. Examination of Figure 2-3 indicates that regardless of the direction of the precession, the same FID is detected. Therefore in this simple detection scheme, only the distance from the resonant and carrier

frequencies is obtained, and not the absolute position. The most important advantages of QD is removing the need to tune the phase of the receiver and the ability to extract all available information from the signal and unambiguously determine the resonant position.

The idea of QD conceptually, is to use two pickup coils oriented at  $90^\circ$  to each other. In this way both the x-component and y-component of the magnetization are detected. The two sets of data represent a complex FID. The Fourier transform of the complex FID unambiguously determines the resonance positions in a spectrum. The real part of the transform represents the absorption spectrum and the imaginary part represents the dispersive spectrum of the nuclear spin system.

In practice, the existence of two coils imposes complications and constraints on the engineering design of the resonant circuit. Fortunately, it can be shown that splitting the radio signal in two and mixing each with carrier frequency's with a relative phase of  $90^\circ$  is equivalent. This process is shown schematically in Figure 2-2.

Obvious challenges with respect to this process are the requirement for a stable and accurate  $90^\circ$  phase shift in the reference and nominally equivalent PSD's. These issues have been solved in current spectrometer technology.

In summary, the main advantage of QD is removing the need to tune the phase of the receiver and unambiguous determination of the resonance position. Additionally, and stated without justification, QD also provides more efficient use of transmit power, and better optimization of signal to noise ratio.

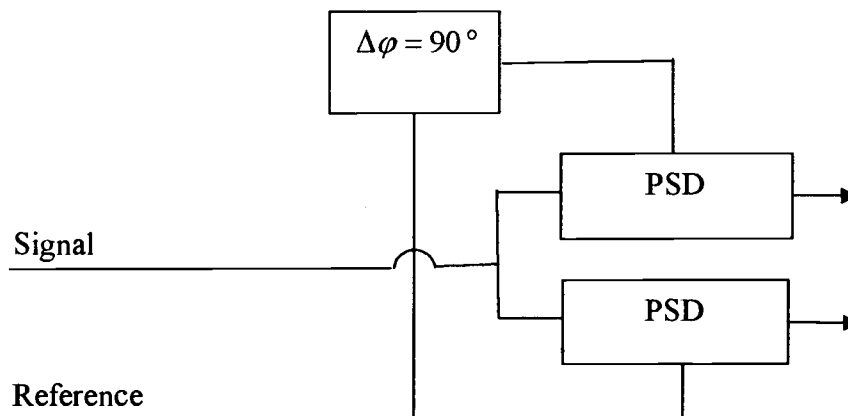
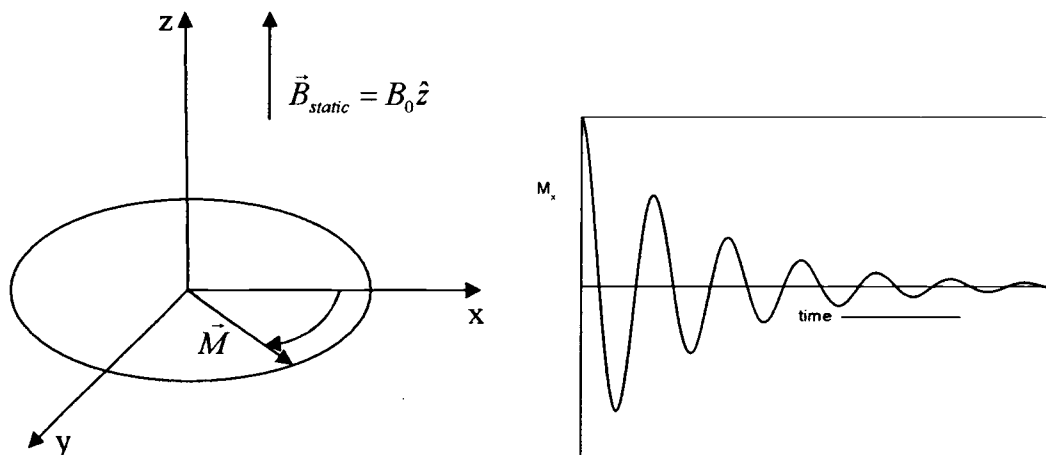
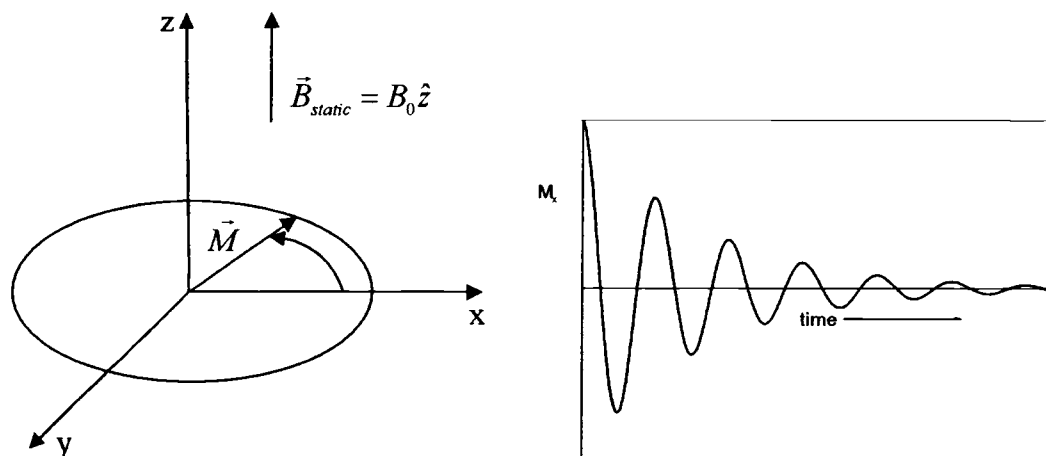


Figure 2-2: Quadrature detection of the NMR signal. The NMR signal is split in two. One part is mixed with the reference signal in the lower PSD (phase sensitive detector), and one part is mixed with the reference signal shifted by  $90^\circ$  in a second PSD. The output of the PSD's goes the ADC's.



(a)



(b)

Figure 2-3: a) Magnetization processing clockwise in the x-y plane of the coil, and the associated FID. b) Magnetization processing counter-clockwise and the associated FID. The FID's in a) and b) are the same.

### 2.6.1.2 Variable Temperature Operation

Variable temperature measurements were executed using a temperature controlled air/nitrogen flow system. Nitrogen is used for low temperature operation, whereas dry air can be used for higher temperatures (typically, room temperature and above). The gas flow system is a Chemagnetics variable temperature accessory. The accessory consists of a gas flow stack used to direct the gas to the sample probe in the magnet, a temperature controller, a temperature sensing device, and a gas flow regulator unit. Variable temperature measurements can be performed with MAS (magic angle spinning) or static conditions. These components and their operation are described in detail in the CMX spectrometer reference manual.

### 2.6.1.3 Solid-Echo Pulse Sequence

It is often the case that the FID (discussed in section 2.6.1.1) is not readily observable. In this situation the decay constant of the signal is large which represents a broad spectrum in the frequency domain. Ringing in the coil of the probe circuit creates a dead time following the excitation pulse, in which no signal can be observed. If the time constant of the FID is similar to the ring down time of the coil, part or all of the FID may be unobservable. This problem is exacerbated by the fact that it is the beginning of the FID that gives the largest magnitude of magnetization, and is also most affected by coil ringing.

Solids are particularly prone to this situation. Inhomogeneities and strong coupling to the lattice are examples of some sources of broadening. Also relevant to data reduction in subsequent discussions, is the effect of anisotropy of quadrupolar and magnetic interactions in powder patterns, the net effect being a broadening of the spectrum.

The problem has been alleviated with the development of spin-echoes<sup>8,9,10,11,12</sup>.

Depending on the system and the type of spin echo, the nuclear spin system is prepared by excitation with a particular pulse sequence. This excitation is done in such a way that at some later time, the magnetization re-focuses, and a signal is observed.

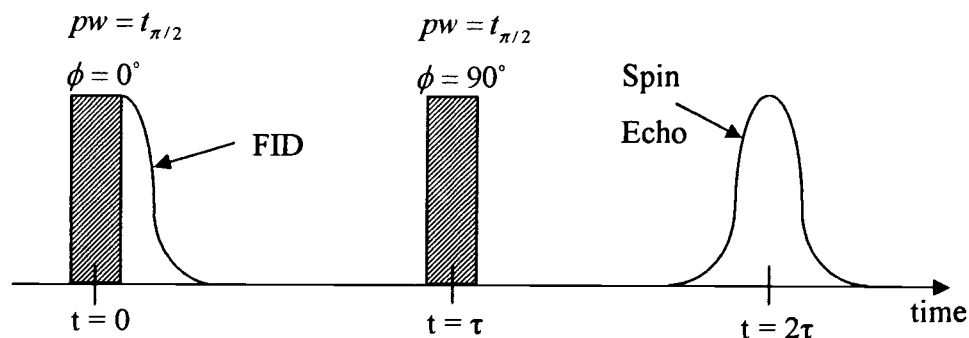


Figure 2-4: Quadrupole echo pulse sequence.

An important pulse sequence used in the current experiments is the quadrupole echo pulse sequence<sup>12</sup>, and is shown in Figure 2-4. The sequence consists of an initial  $\pi/2$  pulse, after which no attempt is made to observe the FID. Then after a time  $\tau$ , which is longer than the de-phasing time of the FID ( $T_2^*$ ), the system is hit with another  $\pi/2$  pulse that is  $90^\circ$  out of phase with the initial pulse. The result is a spin-echo at time  $2\tau$  which is well separated in time from any coil ringing from the pulses. The echo represents two back-to-back FID's.

#### 2.6.1.4 The Probe Circuit

Details of the NMR probe circuit used for all measurements are shown in Figure 2-5. The circuit consists of a sample coil, two tuning capacitors ( $C_{\text{match}}$  and  $C_{\text{tune}}$ ), and two plug in capacitors ( $C_{\text{Bottom}}$ ,  $C_{\text{Top}}$ ). The purpose of the plug-in capacitors is to adjust the tuning range of available resonant frequencies. The exact frequency is then selected out of this range by suitable adjustment of  $C_{\text{match}}$  and  $C_{\text{tune}}$ . The main advantage of this configuration is that it provides an overall wide range of available tuning frequencies. With a standard 6-turn coil, the probe can be tuned from 88MHz to 140MHz. A look up table is used to determine the appropriate combination of plug-in capacitance for a given range of tuning frequencies.

This range can be modified by changing the sample coil, or the inductance in the circuit. For instance, this was required in the case of  $^{67}\text{Zn}$  NMR, where the resonance frequency was about 20MHz.

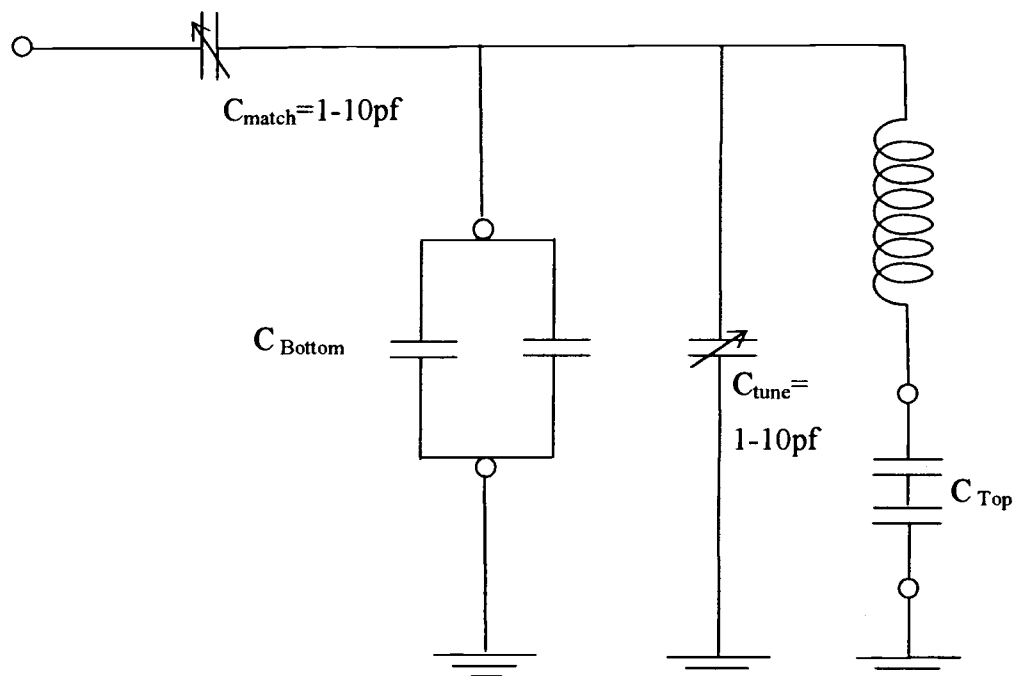


Figure 2-5: Details of NMR probe circuit.

### 2.6.1.5 Magic Angle Spinning

As discussed previously in sections 2.2.1 and 2.2.2, quadrupolar and magnetic interactions are in general anisotropic, meaning that the local hyperfine field is a function of the orientation of the crystal with respect to the applied magnetic field. As a result of the anisotropy of these various interactions, NMR powder patterns (see section 2.4) of solids suffer from broadening. For spin  $I = 1/2$ , the broadening arises mainly from interactions between magnetic dipoles of adjacent nuclei, as well as chemical and/or Knight shift anisotropies when the symmetry is less than cubic. This is explicit in equation 2.44 for the Knight shift, and implicit in equation 2.34 for the

chemical shift. For quadrupolar nuclei,  $I > 1/2$ , additional broadening occurs due to the interaction of the nuclear quadrupole moment and the local electric field gradient, again when the symmetry is less than cubic. This is shown explicitly in equations 2.24 and 2.25 for the first and second order quadrupole effects respectively.

It may be noted that these interactions contain terms in  $(3 \cos^2 \theta - 1)$ , where  $\theta$  is the angle between the principal axis of the interaction and the applied magnetic field.

Therefore when  $\theta = 54.74^\circ$  these terms go to zero and this is called the magic angle. In a powder sample, the orientation of the principal axis of the various crystallites is typically random.

The technique of Magic Angle Spinning (MAS) takes advantage of the magic angle by orienting the entire sample at the magic angle, and spinning the sample rapidly, therefore averaging the interaction about the magic angle. Depending on the strength and symmetry of the interaction and the spinning speed, the broadening effects can be completely or partially reduced.

MAS has been an important technique in solid state NMR. In the study described in the following section, MAS is used on samples to reduce broadening, effectively increasing resolution. This increase in resolution proved critical in the effort to identify inequivalent nuclear sites.

### 3 NUCLEAR MAGNETIC RESONANCE INVESTIGATION OF THE STRUCTURE OF PHASE TRANSITIONS IN THE $ZrV_{2-x}P_xO_7$ SERIES

#### 3.1 Introduction

The purpose of this investigation is the application of NMR to aid in the understanding of the materials  $ZrV_{2-x}P_xO_7$ . The technologically interesting and principal property of these materials is that for certain values of  $x$  they show strong isotropic negative thermal expansion over a wide temperature range. Our goal is to confirm the structure and structural phase transitions observed in these materials that have been reported using various techniques<sup>13</sup>. Figure 3-1 shows the ideal structure for cubic  $A^{4+}M_2^{5+}O_7$  compounds. Reported here are the relevant NMR results and conclusions.

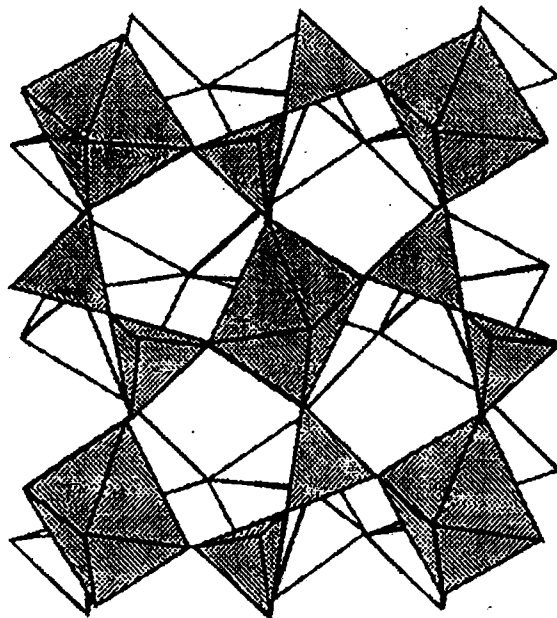


Figure 3-1: Ideal structure for cubic  $A^{4+}M_2^{5+}O_7$  compounds.

Central to this study is the understanding of the room temperature structure of members of the series near the end points ( $x=0$ ,  $x=2$ ). The proposed structure is a  $3 \times 3 \times 3$  superstructure in the space group  $Pa\bar{3}$  in which the cubic cell edges are tripled. This structure results in 11 distinct crystallographic sites for vanadium ( $x=0$ ), or phosphorous ( $x=2$ ), in which 8 of these sites have unit intensity and 3 of the sites have  $1/3$  unit intensity. Above the structural phase transitions the ideal cubic structure is achieved and the space group remains  $Pa\bar{3}$ .

## 3.2 Experimental Techniques

### 3.2.1 Samples

Nuclear magnetic resonance (NMR) with magic angle spinning (MAS) (see section 2.6.1.5) was used to study  $ZrV_{2-x}P_xO_7$  samples with compositions  $x=2.0$ ,  $1.6$ ,  $1.0$ ,  $0.3$ , and  $0.0$ . Described below is a summary of the thermal and structural properties of the beginning, middle, and end members<sup>13</sup>.

$ZrP_2O_7$  shows one phase transition at 290C. Below this transition evidence of superstructure and normal thermal expansion is observed. Above the transition very low and positive thermal expansion is observed. In  $ZrV_2O_7$  two phase transitions near 100C are observed. Below the transitions the thermal expansion is normal and there is evidence for a superstructure. Above the transitions strong isotropic negative thermal expansion commences and continues up to 800°C, where decomposition occurs.

In the mixed material  $ZrVPO_7$  the phase transitions above room temperature are completely suppressed with no evidence of superstructure. Low negative thermal expansion is observed.

### 3.2.2 NMR Techniques

Experiments were carried out using a Chemagnetics CMX360 spectrometer at a spinning frequency of 5 kHz in a magnetic field of 8 Tesla. The  $^{31}P$  spectrum for  $ZrP_2O_7$  spectrum was obtained at a MAS frequency of 18 kHz in a 11.7 Tesla field<sup>14</sup>.

NMR spectra were obtained for both  $^{51}\text{V}$  and  $^{31}\text{P}$ . The  $^{51}\text{V}$  nucleus has a gyromagnetic ratio  $\gamma = 11.19 \text{ MHz/Tesla}$ , a spin  $I=7/2$  and electric quadrupole moment  $Q = -4 \times 10^{-2} \text{ barn}$ . The  $^{31}\text{P}$  nucleus has a  $\gamma = 17.235 \text{ MHz/Tesla}$  and  $I=1/2$ . Variable-temperature NMR (section 2.6.1.2) in the range 25-180C was used to study the structural phase transitions in  $\text{ZrV}_2\text{O}_7$ .

### 3.3 Experimental Results

The proposed  $3 \times 3 \times 3$  superstructure is supported by NMR measurements. The room-temperature  $^{31}\text{P}$  spectrum for  $\text{ZrP}_2\text{O}_7$  at high resolution is shown in Figure 3-2.

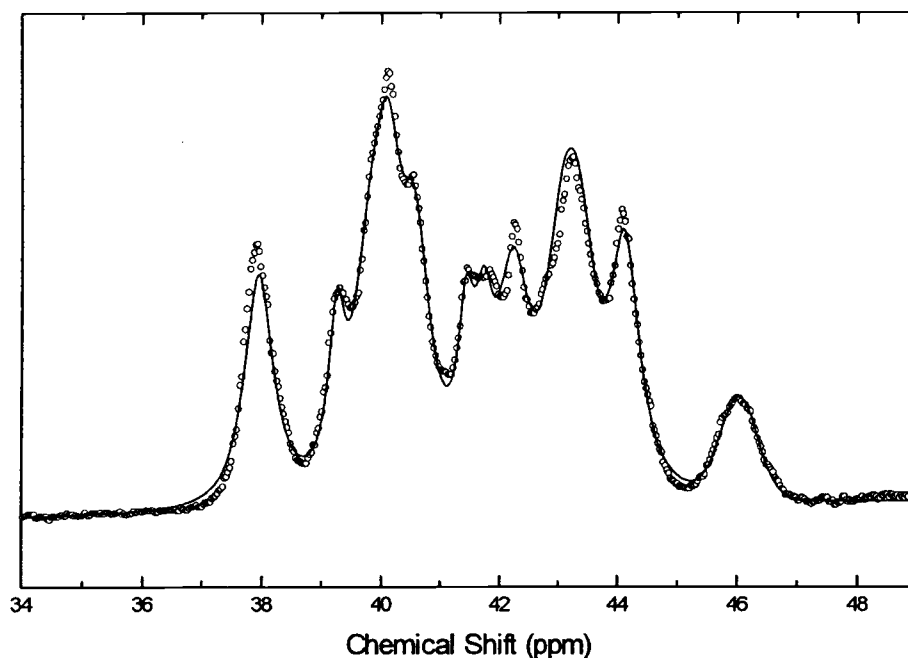


Figure 3-2:  $^{31}\text{P}$  NMR MAS spectrum for  $\text{ZrP}_2\text{O}_7$  at room temperature. The broken line represents the model of 11 mostly Lorentzian peaks and 1 Gaussian peak at 46 ppm. The MAS frequency was 18 kHz, and the chemical shift reference was phosphoric acid.

Superimposed on the data is a least-squares fit to 11 mainly Lorentzian peaks and 1

Gaussian peak at 46 ppm. The fits to the 11 peaks include a small Gaussian admixture. Eight of these peaks were constrained to unit intensity, and three were constrained to one-third unit intensity in accordance with the  $P\bar{a}3$  space group. A preliminary fit in which the line widths of the individual peaks were free parameters showed a systematic tendency for narrower widths for the three less intense lines. In the fit shown in Figure 3-2, the widths of the three (intensity 1/3) lines and the eight (intensity 1) lines were constrained so that the widths could vary by no more than 10% within each group. This procedure is consistent with the expectation that the line widths of closely similar sites should not vary widely. The model fits the data well and is consistent with space group  $P\bar{a}$  and the 3x3x3 superstructure described above. Table 3-1 reports the chemical shift of each peak as determined by the least-squares fit. The Gaussian peak is assumed to be the result of an unknown impurity phase representing 4.4% of the total intensity. This is presumably the same phase giving rise to three weak peaks of an unidentified impurity in the neutron diffraction pattern of  $ZrP_2O_7$ .

Table 3-1:  $^{31}\text{P}$  NMR Parameters for the Series  $\text{ZrV}_{2-x}\text{P}_x\text{O}_7$ 

sample	peak	chemical shift (ppm) <sup>a</sup>	hwhm (ppm)	rel. int
$\text{ZrP}_2\text{O}_7^b$	1	37.93	0.29	1
	2	39.25	0.16	0.33
	3	39.82	0.35	1
	4	40.12	0.28	1
	5	40.57	0.30	1
	6	41.43	0.16	0.33
	7	41.73	0.18	0.33
	8	42.22	0.33	1
	9	43.07	0.35	1
	10	43.35	0.35	1
	11	44.12	0.29	1
	12	46.04	0.36	0.39
$\text{ZrV}_{0.4}\text{P}_{1.6}\text{O}_7$	V-O-P	30.63	2.7	1
	P-O-P	43.46	2.5	3.62
$\text{ZrVPO}_7$	V-O-P	29.98	2.7	4.37
$\text{ZrP}_2\text{O}_7$	P-O-P	43.88	2.5	1
$\text{ZrV}_{1.7}\text{P}_{0.3}\text{O}_7$	V-O-P	28.73	2.4	1

<sup>a</sup> Referenced to phosphoric acid. <sup>b</sup> Peaks 1-11 are a sum of Gaussian and Lorentzian functions. The percent Gaussian intensity and ratio of Gaussian width to Lorentzian width are fit parameters but are constrained to be the same for each line. These numbers are 14.1% and 1.24%, respectively. The relative intensity of these peaks is also constrained to the fit. The width of lines with 0.33 relative intensity are allowed to float in the range  $0.164 \pm 0.0165$ . The width of lines with unit relative intensity are allowed to float in the range  $0.316 \pm 0.0316$ . Peak 12 is purely Gaussian with the intensity, width, and position allowed to float freely. The intensity of this line accounts for 4.4% of the total intensity.

The room temperature  $^{31}\text{P}$  spectrum for  $x=1$  is shown in Figure 3-3.

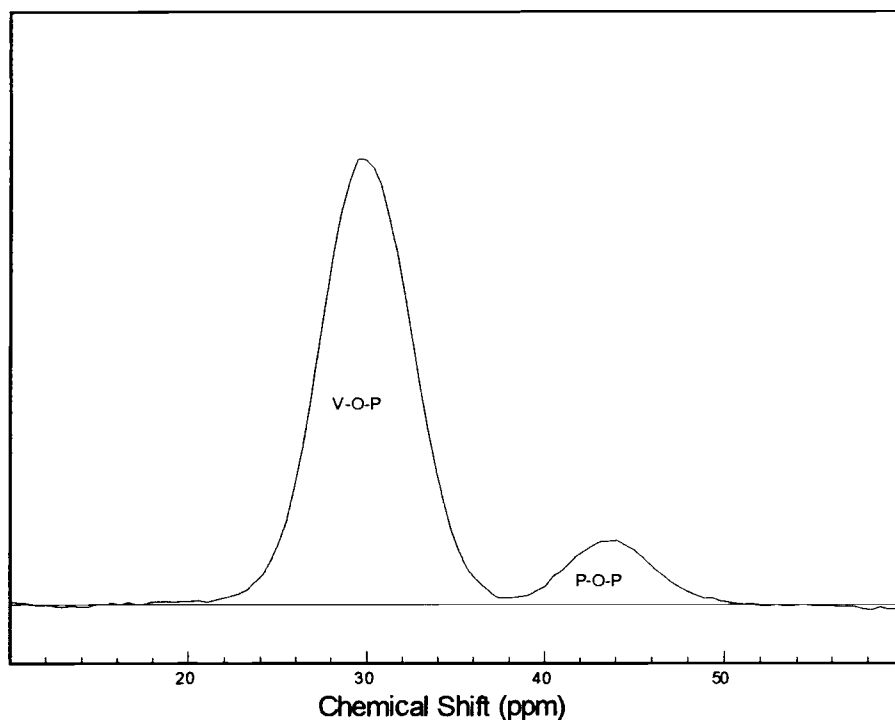


Figure 3-3:  $^{31}\text{P}$  NMR spectrum for  $\text{ZrVPO}_7$  at room temperature.

Two distinct lines are observed. Comparing relative intensities for the various compositions  $x = 2, 1.6, 1.0,$  and  $0.3,$  we have identified the lower chemical shift line as representing phosphorus in a V-O-P bonding configuration and the high shift line as phosphorus in a P-O-P bonding configuration. The ratio of the number of V-O-P to P-O-P bonds was measured to be 0.28 and 4.37 for  $x = 1.6$  and  $1.0,$  respectively. If sites were occupied randomly, these ratios would be 0.5 and 2.0, respectively. Therefore, a mixture of  $\text{P}_2\text{O}_7$  and  $\text{V}_2\text{O}_7$  groups is favored over  $\text{PVO}_7$  groups for  $x = 1.6$  (phosphorous rich), whereas  $\text{PVO}_7$  groups are favored over a mixture of  $\text{P}_2\text{O}_7$  and  $\text{V}_2\text{O}_7$  groups for  $x=1.0$  (equal vanadium and phosphorus content). No P-O-P bonds were observed in the  $x = 0.3$  material. In the mixed materials, no structure is

observed in the NMR spectra. It was not possible to resolve distinct lines for  $V_2O_7$  and  $PVO_7$  groups in the  $^{51}V$  spectra at 8 T.

Figure 3-4 shows the  $^{51}V$  spectra in  $ZrV_2O_7$  at various temperatures. The systematic uncertainty in the sample temperature, due primarily to gradients in the air flow system and calibration errors, is estimated to be  $\pm 5^\circ C$ . It can be seen that evidence of the  $3 \times 3 \times 3$  superstructure remains at  $80^\circ C$ , but this structure is washed out in the  $90^\circ C$  spectrum, consistent with a phase transition in this temperature range. A transition in the  $90-110^\circ C$  is not apparent in the NMR spectra, but a gradual narrowing of the line indicates a single quadrupole-split site at temperatures above  $130^\circ C$ . The 507 Hz splitting in the high-temperature spectrum is characteristic of an axially symmetric quadrupole powder pattern and is consistent with observed first-order quadrupole satellite transitions. A value of the nuclear quadrupole coupling constant,  $\left( \frac{e^2 q Q}{h} \right) = 1.92 \text{ MHz}$  was determined from the satellite splitting. Within experimental uncertainty,  $\left( \frac{e^2 q Q}{h} \right)$  is independent of temperature in the range  $25-180^\circ C$ .

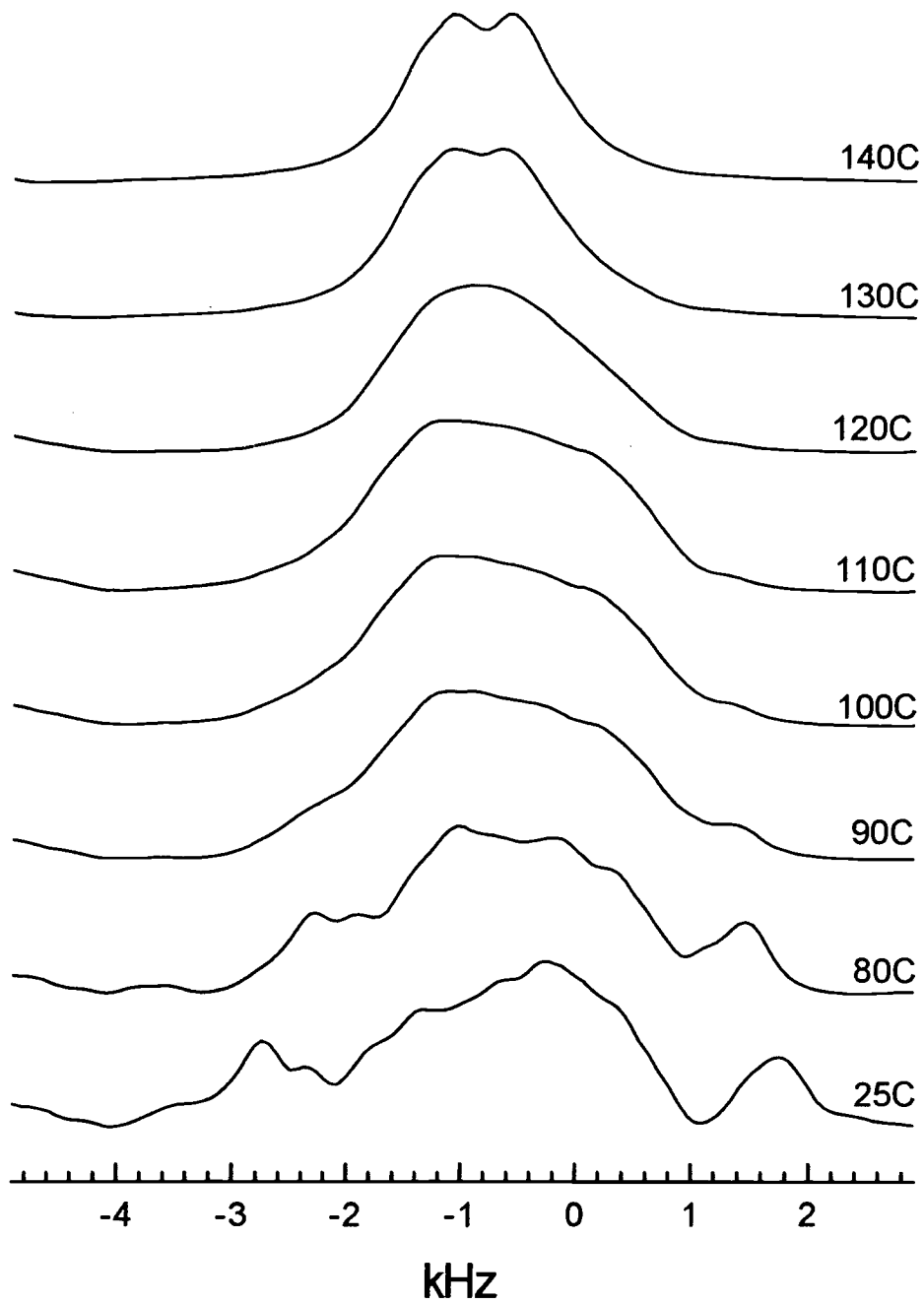


Figure 3-4: 51V NMR spectra at various temperatures.

### 3.4 Conclusions

Analysis of the  $^{31}\text{P}$  spectrum is consistent with the proposed  $3\times 3\times 3$  superstructure in which there exist 11 crystallographic distinct sites for phosphorous. The fact that 8 sites have unit intensity and 3 sites have  $1/3$  unit intensity is maximally constrained in the fit. This spectrum also indicates the presence of an impurity phase that accounts for 4.4% of the total intensity measured with NMR.

$^{51}\text{V}$  variable temperature MAS NMR in  $\text{ZrV}_2\text{O}_7$  exhibits evidence of the  $3\times 3\times 3$  superstructure at room temperature and shows that the ideal structure is reached by  $130^\circ\text{C}$ .

The  $^{31}\text{P}$  spectrum in  $\text{ZrVPO}_7$  shows no evidence of superstructure. However, the V-O-P linkages observed by NMR, suggest a possible mechanism for the suppression of the phase transitions in this material.

## 4 $^{27}\text{Al}$ AND $^{69}\text{Ga}$ IMPURITY NUCLEAR MAGNETIC RESONANCE IN $\text{ZnO}:\text{Al}$ AND $\text{ZnO}:\text{Ga}$

### 4.1 Introduction

Zinc-oxide based materials have many applications including catalysts, luminescent materials, fungicides, surface acoustic wave devices, varistors, and transparent conductors. Transparent conducting powders find important uses as additives to polymers and paper to reduce the build up of static electricity. Zinc oxide based conducting powders have the advantages of low cost and are non-toxic. Bulk transport properties of gallium-doped zinc oxide have been reported<sup>15</sup>. These measurements indicate conductivity values in gallium-doped zinc oxide as high as  $300\text{ S/cm}$ . In this study we attempt to gain an understanding of the local environment of the impurity nuclei, complementing bulk transport studies. Specifically, experimental goals are to determine the locations of group III impurities in the crystal structure, and clarify the nature of electronic states associated with these impurities. Here we report NMR data for gallium, aluminum, and zinc.

### 4.2 Experimental Techniques

#### 4.2.1 Sample Preparation and Characterization

Gallium doped samples were prepared using the reagents gallium metal (4N, Strem Chemicals),  $\text{Ga}_2\text{O}_3$  (5N, Johnson Matthey), and reagent grade  $\text{ZnO}$  (99.7%+, Strem Chemicals). Mixtures were ground together before sealing in predried silica tubes under vacuum, and then heated to  $1200^\circ\text{C}$  for a period of 10 hrs. Starting mixtures contained  $\text{ZnO} + \text{Ga}$  metal for preparation under low oxygen partial pressure, and  $\text{ZnO} + \text{Ga} + \text{Ga}_2\text{O}_3$  for preparation under high oxygen partial pressures. Aluminum doped samples were prepared similarly using appropriate mixtures of the reagents  $\text{Al}_2\text{O}_3 + \text{ZnO}$ .

In this study we perform NMR experiments on three sample series. Two of these can be formulated as  $Zn_{1-x}Ga_xO$ ,  $Zn_{1-x}Al_xO$  and are referred to as the stoichiometric series. A non-stoichiometric series is formulated as  $Zn_{0.98}Ga_{0.02}O_{1+z}$ . In this series the ratio of the metal to oxygen content is varied according to the parameter  $z$ , and the gallium concentration is held constant at 2 at. %. The two stoichiometric series will be designated  $Ga(x)$ , and  $Al(x)$  respectively, where  $x$  is the dopant concentration given in atomic percent to identify a particular sample. The non-stoichiometric series is designated as  $Ga(2)O(z)$ , where  $z$  is the excess oxygen content also given in atomic percent. Table 4-1 lists the samples studied in this investigation with the corresponding impurity concentrations and oxygen content.

Table 4-1: List of samples and associated impurity concentration.

Series	Sample impurity concentration $x$ or oxygen content $z$ (at. %).	Label
$Zn_{1-x}Ga_xO$	0.03	Ga(0.03)
	0.1	Ga(0.1)
	0.3	Ga(0.3)
	0.5	Ga(0.5)
	1.0	Ga(1.0)
	2.0	Ga(2.0)
	2.7 <sup>16</sup>	Ga(2.7)
$Zn_{1-x}Al_xO$	0.1	Al(0.1)
	0.3	Al(0.3)
	0.5	Al(0.5)
	1.0	Al(1.0)
	2.0	Al(2.0)
$Zn_{0.98}Ga_{0.02}O_{1+z}$	-1.2	Ga(2)O(-1.2)
	-0.5	Ga(2)O(-0.5)
	0.3	Ga(2)O(0.3)
	0.6	Ga(2)O(0.6)
	0.9	Ga(2)O(0.9)
	1.0	Ga(2)O(1.0)

#### 4.2.1.1 Summary of Bulk Transport Properties

Characterization of the bulk transport properties for gallium doped zinc oxide have been performed by Wang and others<sup>15,17</sup>. Presented here is a summary of their results.

Conductivity data was obtained on the stoichiometric samples in the impurity concentration range 0.05 – 2.7 at. %<sup>18</sup>. The data indicates the conductivity increases with the impurity concentration throughout the range. The range of conductivities was 300  $S/cm$  at the highest concentration and approximately 0.4  $S/cm$  at the lowest. Additionally, conductivities were measured from 4.2 K to room temperature, with a variation of less than 20%, indicating the samples are in the heavily doped range<sup>19</sup>.

X-ray diffraction results show only clean ZnO patterns with the structural parameters  $c$  and  $a$  increasing by about 0.17% and 0.08% respectively. This is despite the smaller  $Ga^{3+}$  ion compared to  $Zn^{2+}$ .

Hall Effect data<sup>17</sup> and idiometric titration indicate the number of carriers per impurity atom is never greater than 1.

ESR measurements<sup>15</sup> yield a  $g$  value of 1.96 for the conduction band of ZnO, with line broadening as the impurity concentration is increased.

#### 4.2.2 NMR Techniques

NMR measurements were carried out using a Chemagnetics CMX360 spectrometer in a magnetic field of 8 Tesla (unless otherwise indicated) and 5.5 Tesla. The inhomogeneity of the magnet is measured to be a few ppm over the extent of the sample and was negligible in these experiments. The minimum linewidth observed was 33 ppm for the aluminum resonance.

A quadrupolar echo pulse sequence (section 2.6.1.3) was used to obtain spectra for  $^{69}Ga$ ,  $^{71}Ga$ , and  $^{67}Zn$  species in the gallium doped zinc oxide. This was necessary in the case of the gallium resonance where the free induction decay (FID) time  $T_2^*$ , is similar to the receiver dead time. FID's (and corresponding spectra) were obtained for  $^{27}Al$ . In this case, the effect of receiver dead time was not important due to the comparatively longer  $T_2^*$  of the aluminum resonance.

$H_1$  produced by the Chemagnetics NMR probe was measured to be about 600 gauss corresponding to a  $\pi/2$  pulse condition of 2-3 microseconds, depending on the probe

nuclei. In order to achieve a good signal to noise ratio extensive signal averaging was necessary. Typical acquisition counts were in the thousands for aluminum and tens of thousands for gallium and zinc. However, the large acquisition counts for gallium were compensated for by the shorter spin-lattice relaxation rate  $T_1$ , rendering total experiment times reasonable. Variable temperature measurements were done using a CMX air flow system supplied with the spectrometer (section 2.6.1.2). Table 4-2 lists the gyromagnetic ratio, spin, electric quadrupole moment, and natural abundance for these isotopes.

Table 4-2: Properties of NMR isotopes.

NMR isotope	$\gamma$ (MHz/Tesla)	Spin (I)	Q (multiples of barns, $10^{-24}$ cm)	Nat. Ab. (%)
$^{69}\text{Ga}$	10.22	3/2	0.178	60.4
$^{71}\text{Ga}$	12.984	3/2	0.112	39.6
$^{67}\text{Zn}$	2.663	5/2	0.15	4.11
$^{27}\text{Al}$	11.094	5/2	0.149	100

### 4.3 Experimental Results

In this section, the raw experimental data and observations are presented. The NMR parameters which characterize the resonance behavior are the resonance shift, the width and structure of the spectrum (specifically the absorption spectrum), and the spin-lattice relaxation rate  $1/T_1$ .

Resonance shifts are measured with respect to the standard references  $\text{GaCl}_3$ ,  $\text{AlCl}_3$  and  $\text{ZnSO}_4$ , all in dilute aqueous solution.

Due to the anisotropic and disordered nature of the system the definition of the resonance frequency can be elusive due to the complex line shape. Therefore the error bars include this uncertainty. When appropriate, particularly for low S/N, the line widths were measured by fitting the spectra to a sum of gaussians in order to accurately represent them. Spin-lattice relaxation rates were measured by the method of inversion recovery or saturation recovery.

### 4.3.1 Interpretation of Spectra

Figure 4-1 shows  $^{67}\text{Zn}$  spectra in samples pure ZnO, Ga(0.03), and Ga(2) in a field of 8 Tesla.

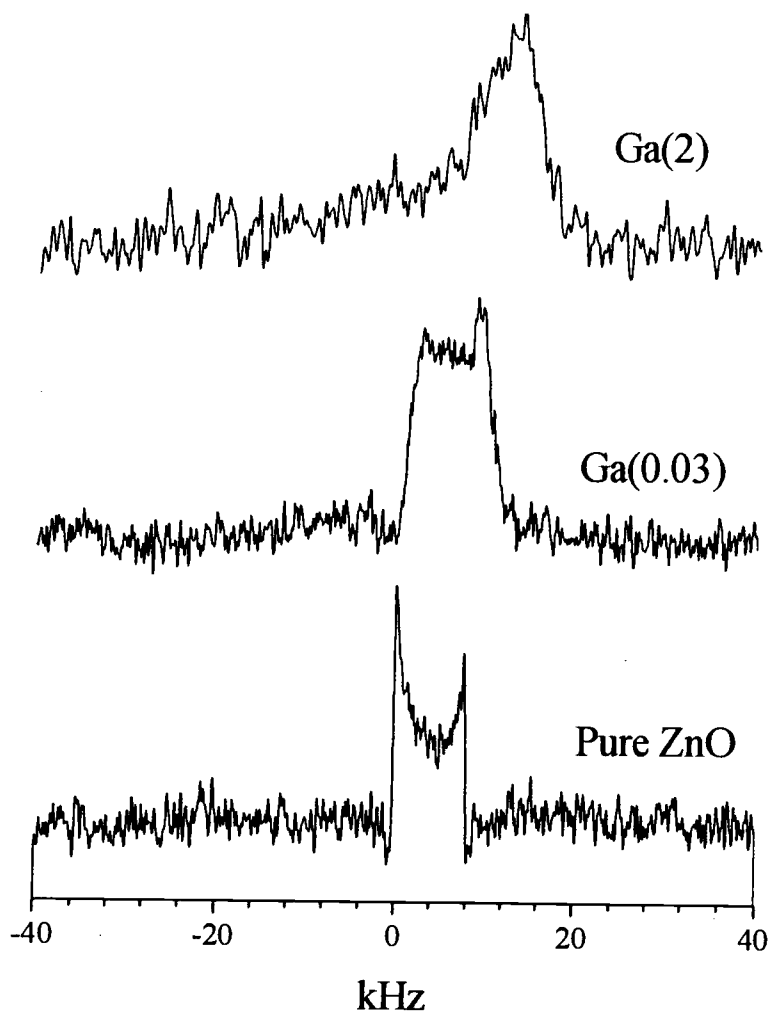


Figure 4-1: Zn spectra in pure zinc oxide, sample Ga(0.03), and sample Ga(2), in a magnetic field of 8 Tesla. The spectrum for pure zinc oxide represents an axial quadrupole powder pattern.

The  $^{67}\text{Zn}$  spectrum in pure zinc oxide is in agreement with previous results<sup>20</sup>, which characterize the spectrum as an axial quadrupole powder pattern from which the

quadrupole coupling constant is reported to be  $(e^2qQ/h)_{67} = 2.35 \pm 0.05 \text{ MHz}$ .

Therefore, the nearest satellite transitions ( $\pm 3/2 \rightarrow \pm 1/2$ ) have a peak in amplitude offset 350 kHz from the central transition with the total intensity distributed throughout the interim. The separation of the singularities is

$\Delta\nu_{1/2 \rightarrow -1/2} = 8.22 \pm 0.15 \text{ kHz}$  corresponding to a quadrupole coupling

$(e^2qQ/h) = 2.38 \pm 0.02 \text{ MHz}^\dagger$  in agreement with previous results.

Doping zinc oxide with gallium has a large effect on the shape of the  $^{67}\text{Zn}$  resonance. Additionally, this effect appears to have strong concentration dependence. The spectrum in sample Ga(0.03) is slightly broadened as might be expected upon introducing disorder in the lattice. However, it retains the square-ness that can be associated with an axial powder pattern. The FWHM is 9.5 kHz. The spectrum in sample Ga(2) loses this square-ness and possibly develops a shoulder protruding on the low frequency side. The FWHM is 8.5 kHz. Therefore no significant change in the width of the resonance is observed. The electric field gradient (EFG) at the nuclear site is characterized by the asymmetry parameter  $\eta \equiv (V_{xx} - V_{yy})/V_{zz}$ , and the magnitude of the quadrupole coupling  $eq \equiv V_{zz}$ .  $\eta$  determines the positions of the peaks and  $eq$  the overall width of the line shape. If the shape is assumed to result from quadrupole interactions alone, the spectra indicate that the addition of gallium impurity leads to asymmetry at the nuclear site and little change in the average magnitude of the EFG.

Figure 4-2 shows a series of  $^{69}\text{Ga}$  spectra at 5.5 Tesla spanning the range of dopant concentration studied.

---

<sup>†</sup> For spin 3/2:  $e^2qQ/h = \sqrt{\nu_0 \Delta\nu}$ .

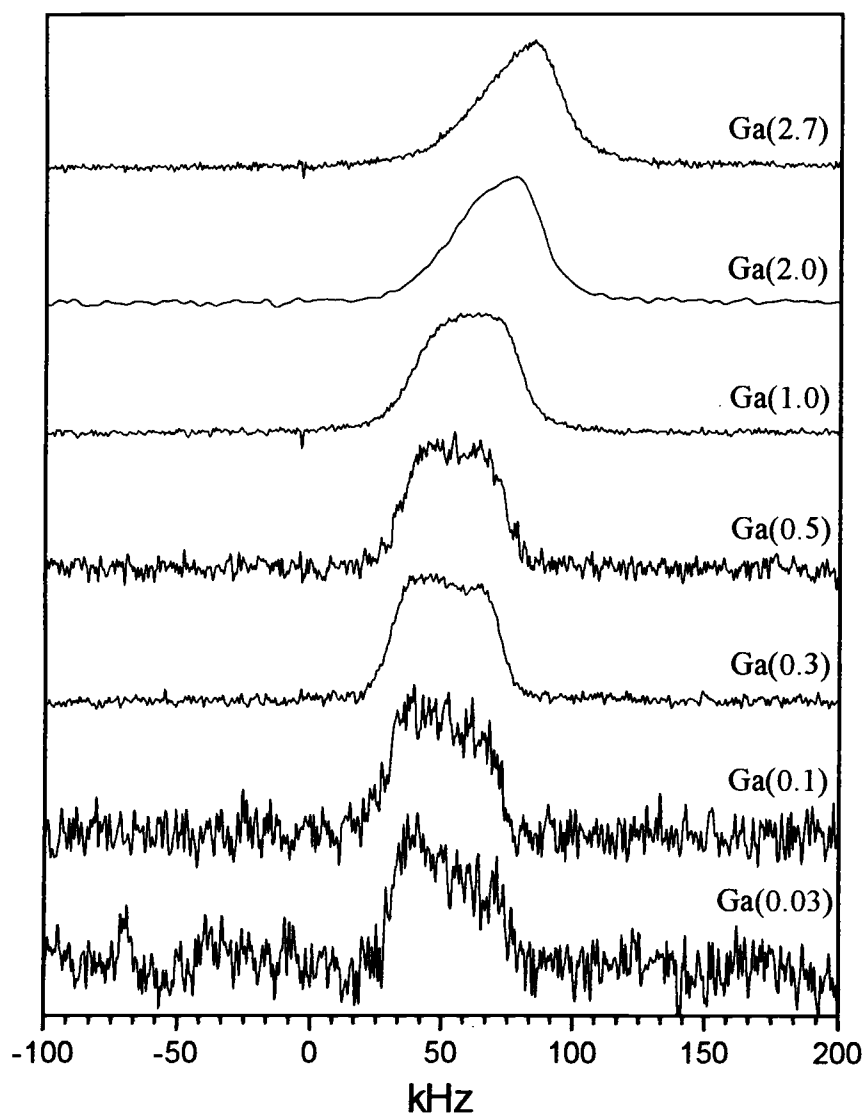


Figure 4-2:  $^{69}\text{Ga}$  spectra in gallium doped zinc oxide at various concentrations in a magnetic field of 5.5 Tesla.

A field of 5.5 Tesla was chosen in these samples to emphasize quadrupole structure, since the splitting of the singularities varies inversely with the applied field. The spectrum for the lowest concentration (sample Ga(0.03)) is identified as an axial quadrupole powder pattern. The characteristic singularities are severely broadened

but there is enough structure remaining to estimate the quadrupole coupling constant,  $(e^2qQ/h) = 3.9(3)MHz$ . As the dopant concentration is varied the spectrum undergoes a continuous change, losing structure associated with an axial powder pattern as the concentration is increased. In sample Ga(2.7) the spectrum is an asymmetric peak with the wide side extending to lower frequencies. The FWHM is 42kHz in sample Ga(0.03) and 34kHz in sample Ga(2.7). The trend is therefore a loss of quadrupole structure with some narrowing of the line as the concentration is increased.  $^{69}Ga$  NMR spectra were also obtained at 8 Tesla although changes in the line shape are much less apparent. The axial line shape of  $^{69}Ga$  in sample Ga(0.03) and the similarity in the trends of the line shapes for  $^{67}Zn$  and  $^{69}Ga$  is strong evidence that gallium occupies  $Ga_{Zn}$  substitution sites.

Figure 4-3 shows a table of spectra for  $^{69}Ga$  and  $^{71}Ga$ . The top row is spectra at 8 T and bottom row is spectra at 5.5T. In column 1 are spectra obtained from sample Ga(0.03), column 2 from samples Ga(0.03) (bottom) and Ga(0.1) (top), columns 3 and 4 from sample Ga(2). The isotope is the same within a given column. Spectra (row=2,column=1) and (2,3), also shown in Figure 4-2, are repeated here for comparison.

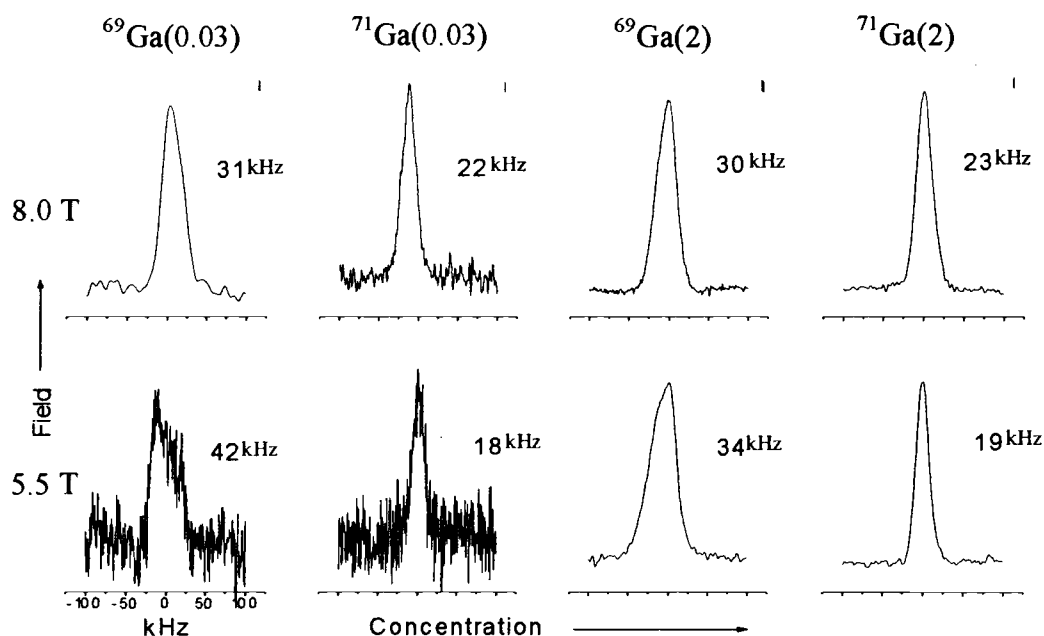


Figure 4-3: Comparison of spectra between both gallium isotopes at 5.5 T and 8 T at low and high dopant concentrations. The number to the right of each spectrum is the FWHM in kHz

Spectra for  $^{71}\text{Ga}$  are nearly independent of concentration. However, there is a slight field dependence, the width increasing with an increase in the field.

Spectra for  $^{69}\text{Ga}$  show a much stronger dependence on field and concentration. For a given concentration the line narrows as the field is increased, which is the opposite of the trend for  $^{71}\text{Ga}$  spectra. This trend is more pronounced in the low concentration sample, where at low field quadrupole structure is clearly evident, but at high field the line appears structureless except for a slight asymmetry. The concentration dependence, shown in detail in Figure 4-2 on width and structure is less pronounced at 8 T than at 5.5 T.

At all concentrations for both 8 T and 5.5 T,  $^{69}\text{Ga}$  spectra are broader than  $^{71}\text{Ga}$  spectra.  $^{71}\text{Ga}$  spectra appear to be devoid of any structure.

Figure 4-4 is a table of time-domain spin-echoes from which the spectra in Figure 4-3 were obtained.

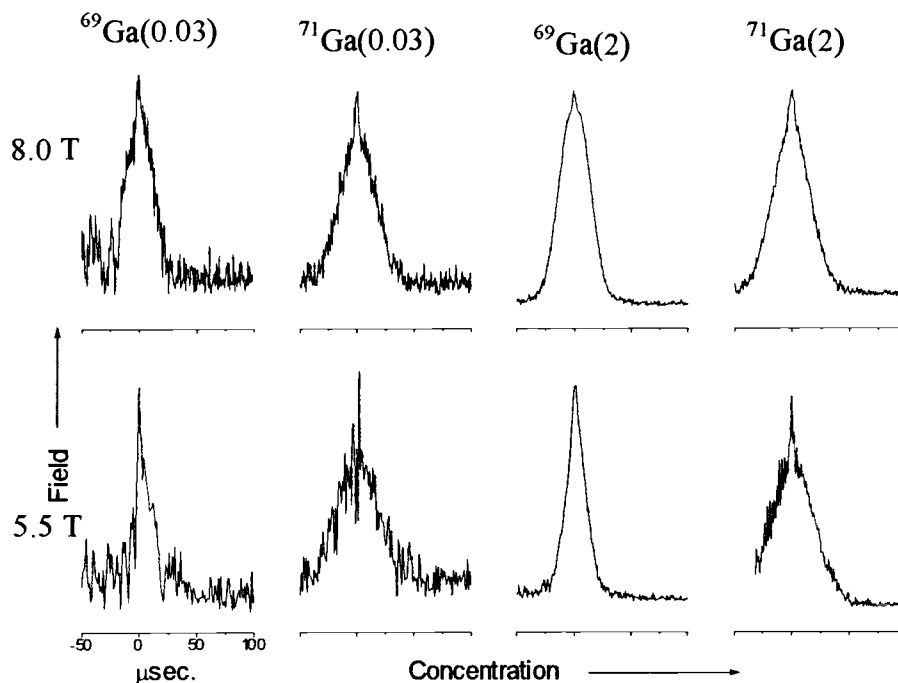


Figure 4-4: Comparison of time-domain spin-echoes between both gallium isotopes at 5.5T and 8T at low and high dopant concentrations.

At 8 T, the shape of the spin-echoes consist of a broad base (narrow line in the frequency domain) on which a sharp peak (broad line in the frequency domain) rests. This time domain signal is expected in the case of a second order quadrupole split powder pattern where the sharp peak represents a small contribution to the magnetization from the satellite transitions. Based on estimates of the quadrupole coupling constant given above for sample Ga(0.03), the contributions to the magnetization from the satellite transitions is calculated to be about  $9 \pm 1\%$ . This compares to the measured value of  $11 \pm 1\%$ . Only the central transition is observed in the frequency domain due to the very broad distribution of the satellites. Spectra for  $^{27}\text{Al}$  can be characterized as relatively narrow (about 30ppm) featureless lines, which yielded no conclusions and are not shown here.

### 4.3.2 Resonance shifts

Resonance shifts were measured for  $^{67}\text{Zn}$  and  $^{69}\text{Ga}$  in the series  $\text{Ga}(x)$ , and  $^{27}\text{Al}$  in series  $\text{Al}(x)$ .

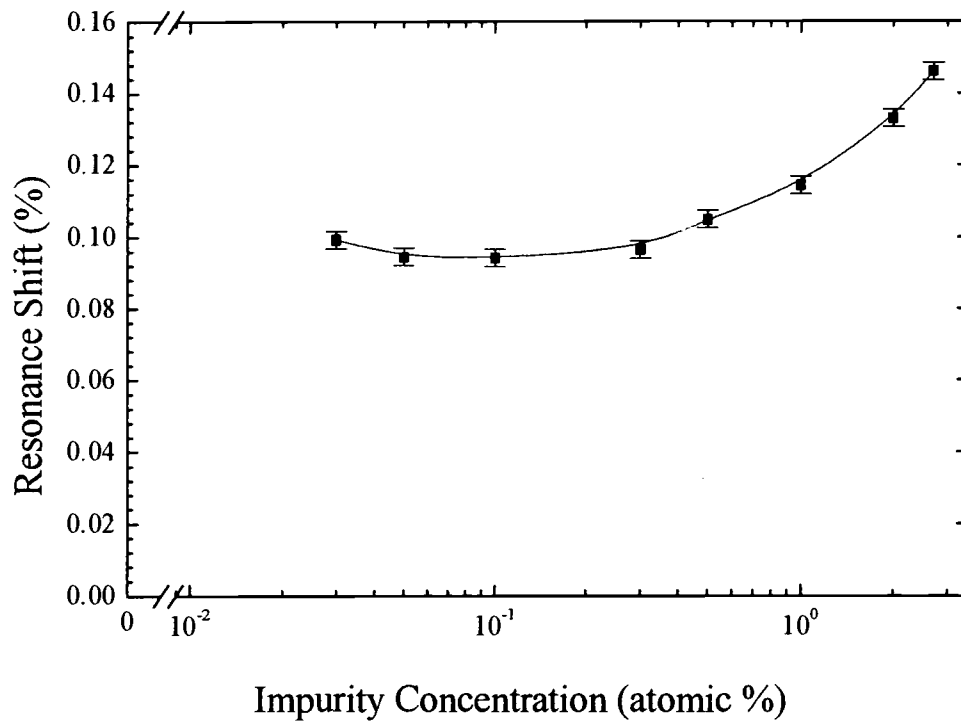


Figure 4-5: Resonance shift vs. dopant concentration of  $^{69}\text{Ga}$  in sample series  $\text{Ga}(x)$ .

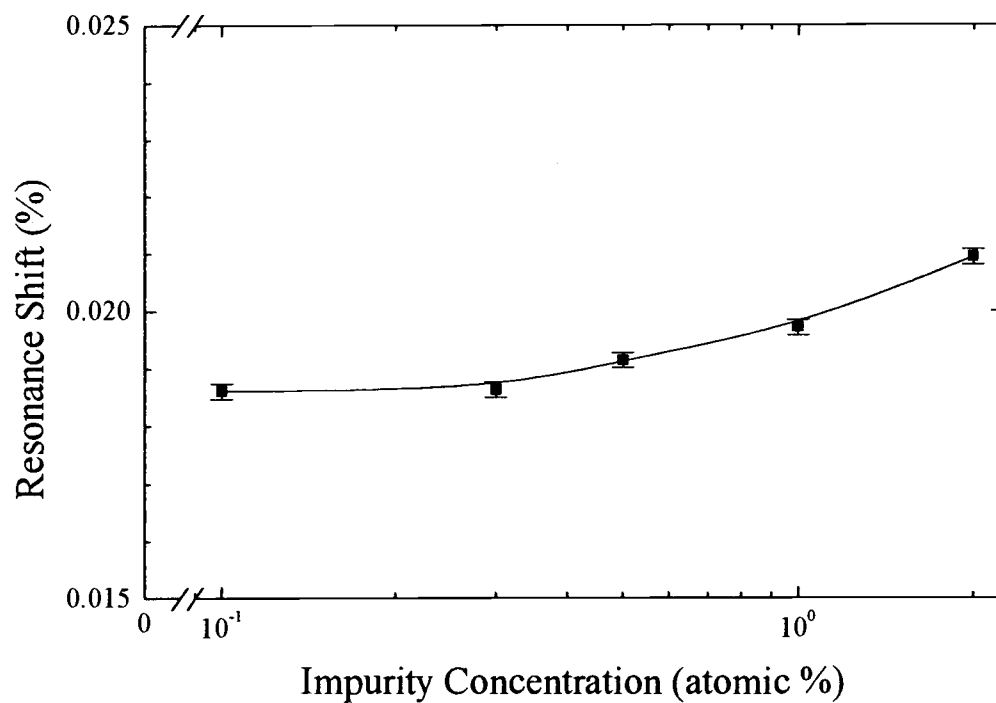


Figure 4-6: Frequency shift vs. dopant concentration of  $^{27}\text{Al}$  for sample series Al(x).

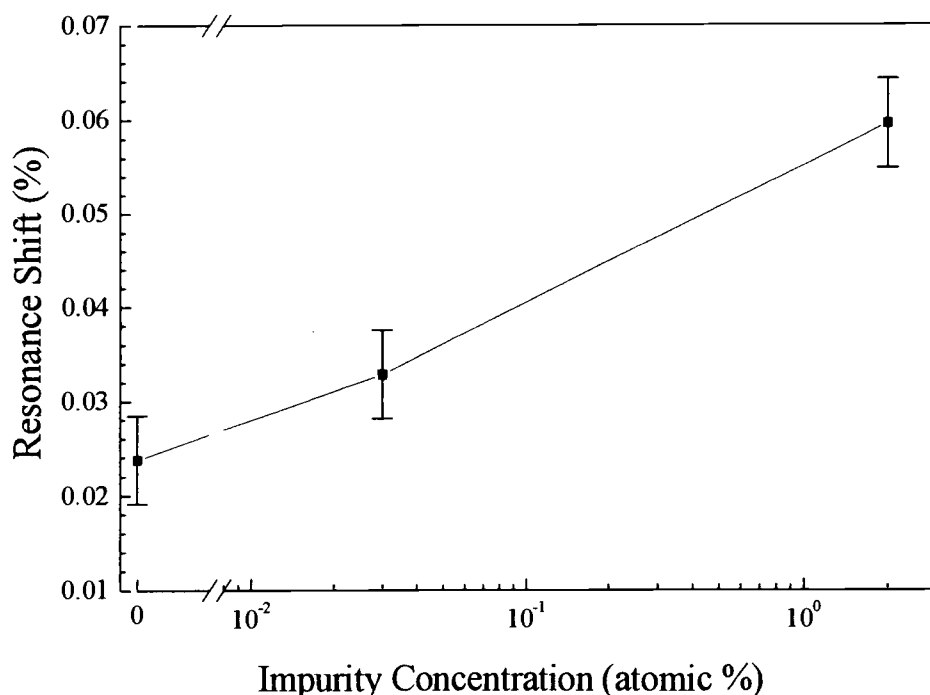


Figure 4-7: Frequency shift of  $^{67}\text{Zn}$  vs. dopant concentration in samples pure ZnO, Ga(0.03), and Ga(2).

All resonance shifts are paramagnetic. Variable temperature measurements on samples Ga(0.03), Ga(1), Ga(2), Ga(3), and Al(2), indicate that the shift is independent of temperature within experimental uncertainty in the range 25C to 200C.

Results for  $^{69}\text{Ga}$  at 5.5T and 8T were the same within experimental uncertainty, indicating the shift is independent of field in that range. Comparison of results for  $^{69}\text{Ga}$  and  $^{27}\text{Al}$  indicates the shift increases with increasing  $Z$ , the nuclear charge. Specifically, the shift for gallium is 5 to 7 times larger than that of aluminum. These basic observations are consistent with the properties of resonance shifts in simple metals, where the dominate contribution is the magnetic hyperfine interaction with intinerant electrons.

In Figure 4-5 the shift is plotted versus impurity concentration for  $^{69}\text{Ga}$  in sample series Ga(x). The data show strong concentration dependence at high concentration ( $>0.1$  at. %), the shift increasing with increasing concentration. At lower concentrations the shift becomes independent of concentration, with a small increase at the lowest concentration measured.

Figure 4-6 plots shift versus impurity concentration for  $^{27}\text{Al}$  in sample series Al(x). The results are similar to that of gallium.

Figure 4-7 plots shift versus impurity concentration for  $^{67}\text{Zn}$  in sample series Ga(x). Only 3 data points were measured indicating the trend of increasing shift with increasing concentration.

### 4.3.3 Spin-Lattice Relaxation

Spin-lattice relaxation rates ( $1/T_1$ ) were measured for  $^{69}\text{Ga}$  in sample series Ga(x), and  $^{27}\text{Al}$  in series Al(x) as a function of x. Measurements were performed at room temperature in a magnetic field of 8 Tesla. Measurements were performed using the method of inversion recovery.  $^{69}\text{Ga}$  Spectra were analyzed assuming a second order quadrupole powder pattern, for which only the central transition is excited (e.g. we are neglecting the contribution to the magnetization from the satellite transitions) and the dominant relaxation mechanism is magnetic in origin. We are led to the latter assumption based on the behavior of the resonance shifts (section 4.3.2) and comparison the between  $^{69}\text{Ga}$  and  $^{71}\text{Ga}$  (discussed below in this section). In this case the magnetic relaxation is described by the 2-component exponential (section 2.5),

$$M(t) = (M(0) - M_{eq})[0.1 \exp(-t/T_1) + 0.9 \exp(-6t/T_1)] + M_{eq}. \quad (4.1)$$

$1/T_1$  was then extracted with a non-linear least squares fit to the raw data.  $^{27}\text{Al}$  spectra were analyzed with a simple single exponential recovery since no quadrupole structure is observed.

In Figure 4-8,  $1/T_1$  for  $^{69}\text{Ga}$  vs. impurity concentration is plotted. The data shows a strong concentration dependence at high concentrations ( $>0.1$  at. %). At low concentrations the rate becomes independent of the concentration, and then increasing slightly for the lowest concentration measured (0.03%). The overall behavior mimics that of the resonance shifts.

Similar results are reported for  $^{27}\text{Al}$  in Figure 4-9. The rate is 40 to 60 times greater for gallium than for aluminum.

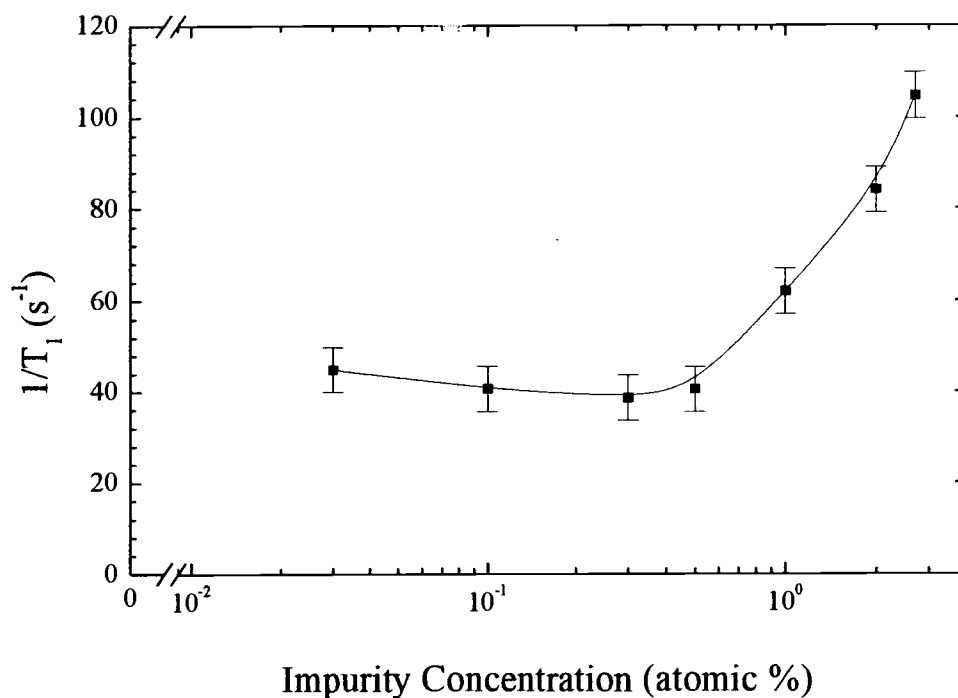


Figure 4-8:  $^{69}\text{Ga}$  spin-lattice relaxation rate vs. impurity concentration in sample series Ga(x).

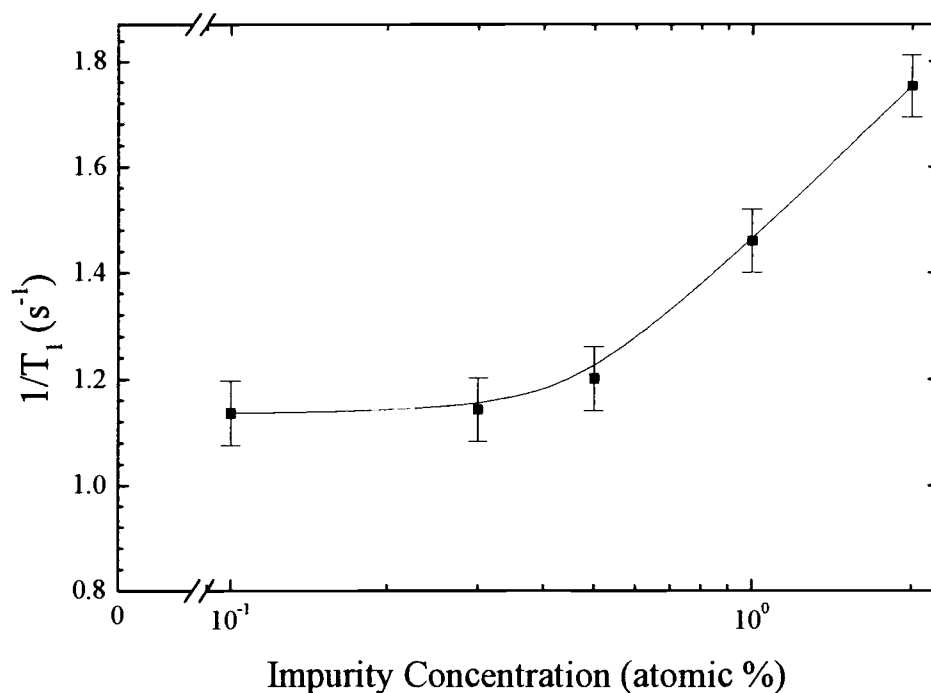


Figure 4-9:  $^{27}\text{Al}$  spin-lattice relaxation rate vs. impurity concentration in sample series Al(x).

Figure 4-10 and Figure 4-11 show the spin lattice relaxation rates of  $^{69}\text{Ga}$  in samples Ga(1), Ga(2), Ga(3), and  $^{27}\text{Al}$  in sample Al(2) at various temperatures. Superimposed on the data is a linear fit, indicating that the rate is nearly proportional to the temperature in the range studied. The relaxation rates are consistent with the linear temperature dependence expected for nuclei coupled to degenerate electron systems.

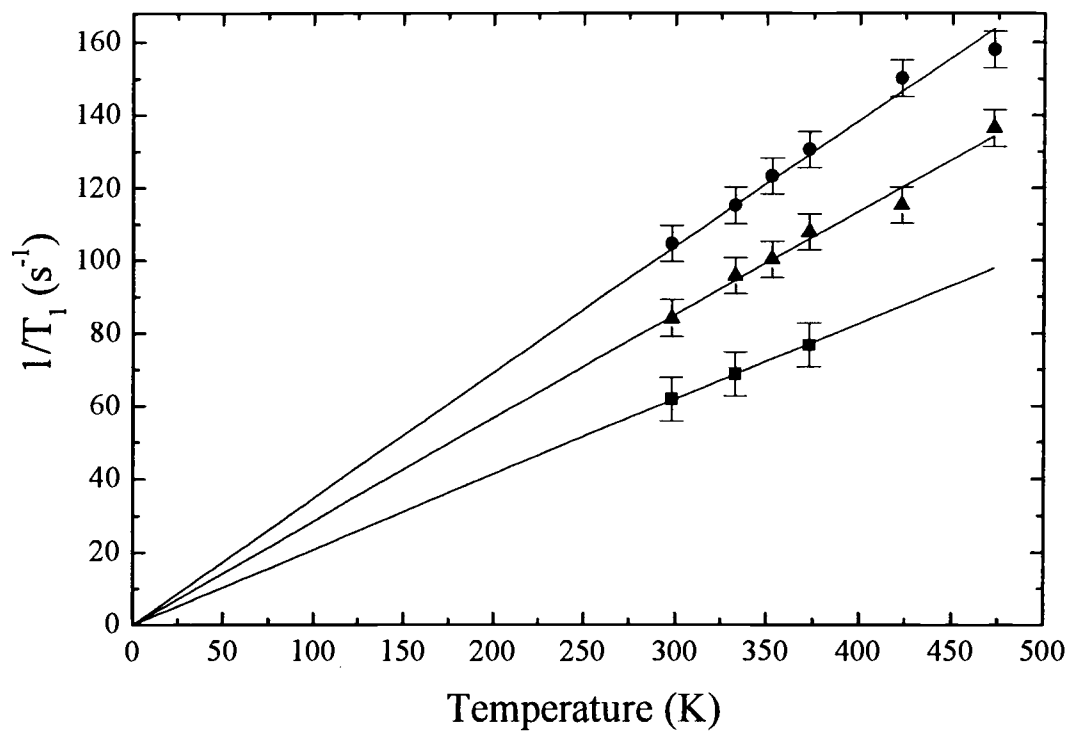


Figure 4-10: <sup>69</sup>Ga spin-lattice relaxation rate vs. temperature in samples Ga(3), Ga(2), and Ga(1).

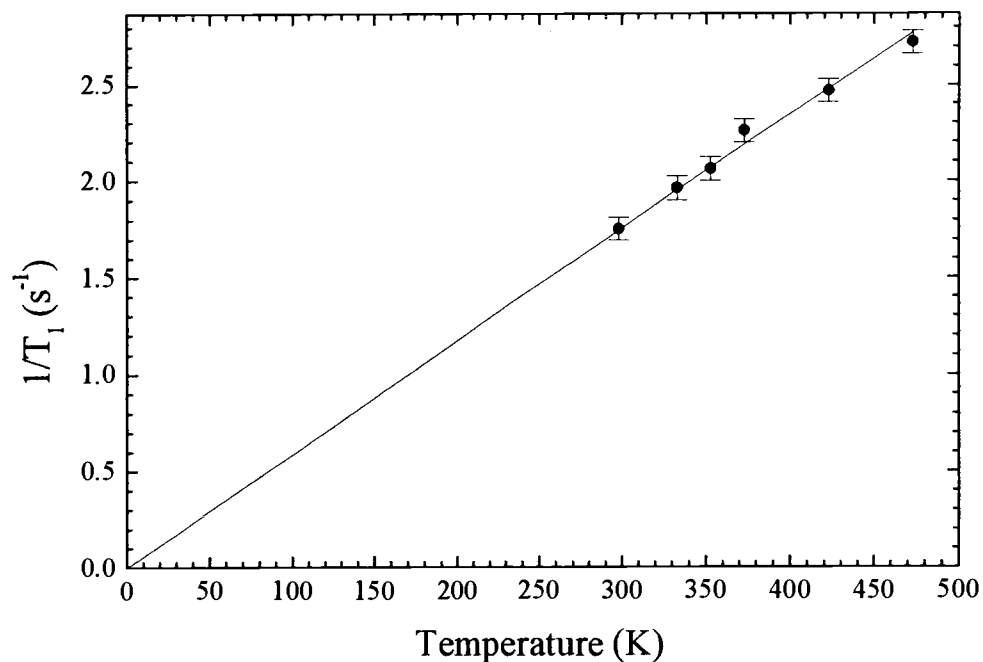


Figure 4-11:  $^{27}\text{Al}$  spin-lattice relaxation rate vs. temperature for sample Al(2).

Additionally, the relaxation rate was measured for  $^{71}\text{Ga}$  in sample Ga(0.1) at 25 °C, yielding  $(1/T_1)_{71} = 63.1 \pm 6 \text{ s}^{-1}$ . This compares to a rate of  $(1/T_1)_{69} = 40.6 \pm 5 \text{ s}^{-1}$  for  $^{69}\text{Ga}$  in the same sample. Comparing the ratio of these values to the ratio of the square of the gyromagnetic ratios of the isotopes gives,

$$\frac{\left(\frac{1}{T_1}\right)_{71}}{\left(\frac{1}{T_1}\right)_{69}} = 1.55 \pm 0.24 \quad (4.2)$$

$$\left(\frac{\gamma_{71}}{\gamma_{69}}\right)^2 = 1.614$$

This indicates the dominant relaxation process is magnetic even at low impurity concentrations, and additionally, justifies the choice of magnetization recovery curve from which the spin-lattice relaxation rate is extracted. This is important due to the fact that the quadrupolar interaction will contribute to relaxation. If quadrupole relaxation contributes significantly, the form of the recovery curve will be different than when magnetic relaxation dominates.

Although the aluminum spectra are essentially featureless, the consistency in the resonance shift and relaxation behavior with that of gallium, naturally lead to the conclusion that aluminum is also substitutional for zinc.

#### 4.3.4 $Zn_{0.98}Ga_{0.02}O_{1+z}$ Series

The  $Zn_{0.98}Ga_{0.02}O_{1+z}$  series represent samples with varying ratios of oxygen to metal content. The concentration ratio of gallium to zinc content is 2 at. % gallium in all samples. Positive  $z$  therefore indicates excess oxygen, and negative  $z$  represents oxygen deficient samples. This is the "nonstoichiometric"  $Ga(2)O(z)$  series. The series is comprised of six samples with  $z$  ranging from -1.2 at. % to 1 at. % (-0.012 to 0.01). Figure 4-12 shows  $^{69}Ga$  time-domain spin-echoes in series  $Ga(2)O(z)$  for different values of  $z$ .

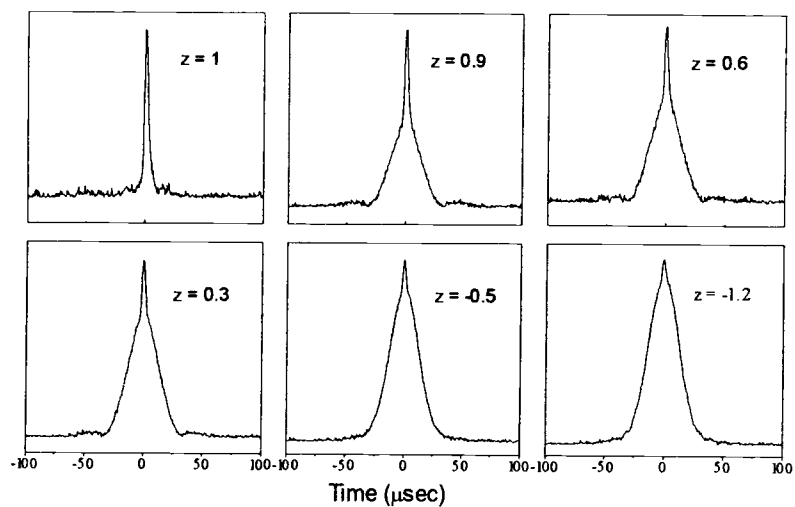


Figure 4-12:  $^{69}\text{Ga}$  time domain spin-echoes vs.  $z$  in atomic percent. The oxygen pressure decreases from left to right and top to bottom.

Figure 4-13 shows the time-domain spin-echo in sample Ga(2) (nominally  $z = 0$ ) for comparison.

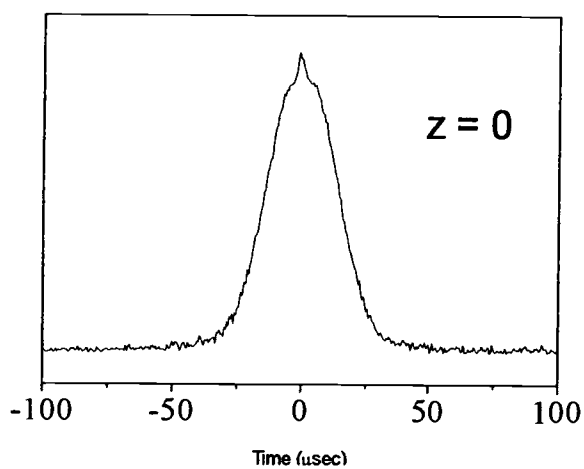


Figure 4-13:  $^{69}\text{Ga}$  time domain spin-echo for sample Ga(2) ( $\text{Zn}_{0.98}\text{Ga}_{0.02}\text{O}$ ).

In general, the shape of the spin-echoes consist of a broad base (narrow line in the frequency domain) on which a sharp peak (broad line in the frequency domain) rests. There is little difference in the signals for  $z = 0, -0.5, -1.2$ . However, for positive  $z$  the trend is a relative increase in the magnetization associated with the sharp peak compared to the broad base. The explanation for such an effect is observation of a second gallium site which becomes more prominent as oxygen content increases. Therefore, Figure 4-12 shows two sites for gallium manifest by the existence of a narrow line (site 1: broad base of the time domain spin echo), and a broader line (site 2: sharp peak in the time domain echo). As mentioned previously, the sharp peak likely has contributions from the satellite transitions. However, this does not explain the relative increase in the contribution to the magnetization from that feature. Further analysis will reveal that site 1 is the site observed in the stoichiometric samples, and site 2 is not definitively identified. The time domain echoes show the trend in the data most clearly: as the oxygen content is increased the relative amount of site 2 increases. Site 2 is not readily observable in the frequency domain except in sample Ga<sub>2</sub>O(1), the most oxygen-rich sample.

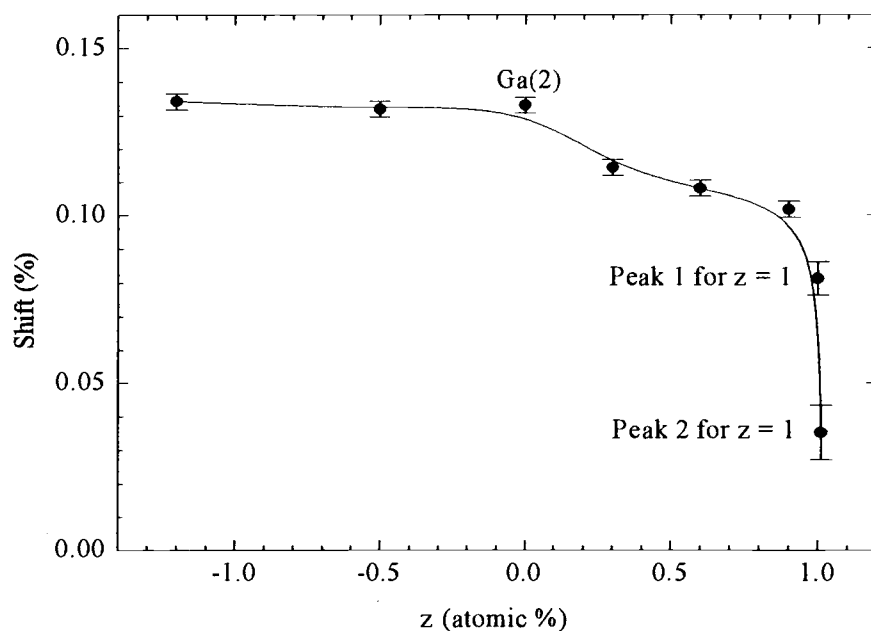


Figure 4-14: Shift of  $^{69}\text{Ga}$  vs.  $z$  for sample series  $\text{Ga}(2)\text{O}(z)$ . Included for comparison is the shift for sample  $\text{Ga}(2)$  (nominally  $z = 0$ ).

Resonance shifts for  $^{69}\text{Ga}$  for varying  $z$  are plotted in Figure 4-14. All shifts are for site 1 (the site observed in the stoichiometric samples), except in  $\text{Ga}(2)\text{O}(1)$  where it was possible to distinguish the two sites in the frequency domain. The shift decreases with increased oxygen content in oxygen rich samples but is approximately independent of oxygen content in oxygen deficient samples. The range of values for the shift of site 1 is similar to that of the stoichiometric samples where the gallium content is varied. Site 2 has a much smaller shift. The line width for site 1 was estimated to be  $30 \pm 5$  kHz, again consistent with the substitutional site observed in the stoichiometric samples. The apparent width for site 2 is about 108 kHz, which may be limited by the pulse spectrum<sup>21</sup>. No attempt was made to better characterize the spectrum of site 2, due to the long experiment times involved.

Figure 4-15 shows the spin-lattice relaxation rate of  $^{69}\text{Ga}$  vs. oxygen content for samples in this series.

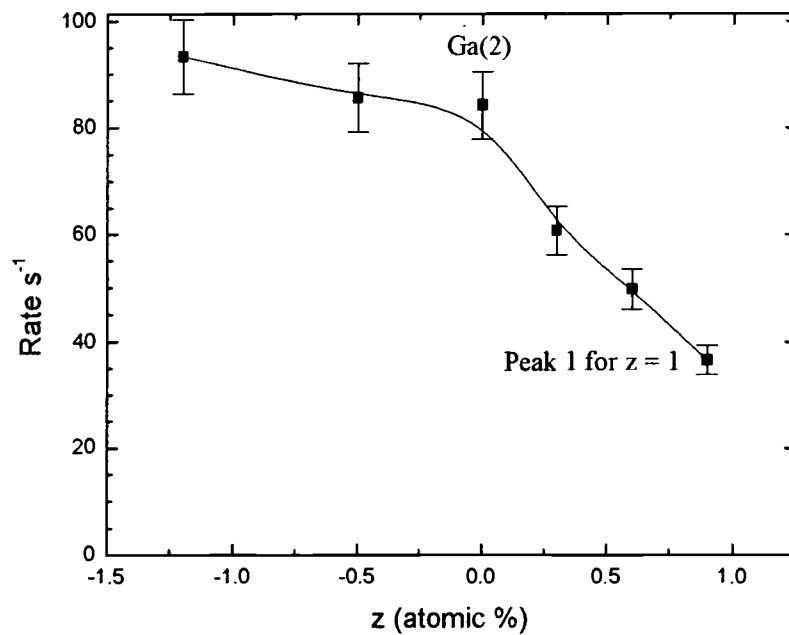


Figure 4-15:  $^{69}\text{Ga}$  spin-lattice relaxation rate vs.  $z$ .

The effect on the rate due to site 2 is small (this is discussed later). The magnitudes of the rates for site 1 are again, consistent with the site observed in the stoichiometric series.

Figure 4-16 shows the spectrum for  $^{71}\text{Ga}$  in sample  $\text{Ga}(2)\text{O}(1)$ . This isotope enabled better resolution of the sites 1 and 2, because of the smaller quadrupole broadening. Figure 4-17 plots the integrated intensity for each site versus the relaxation time after saturation.

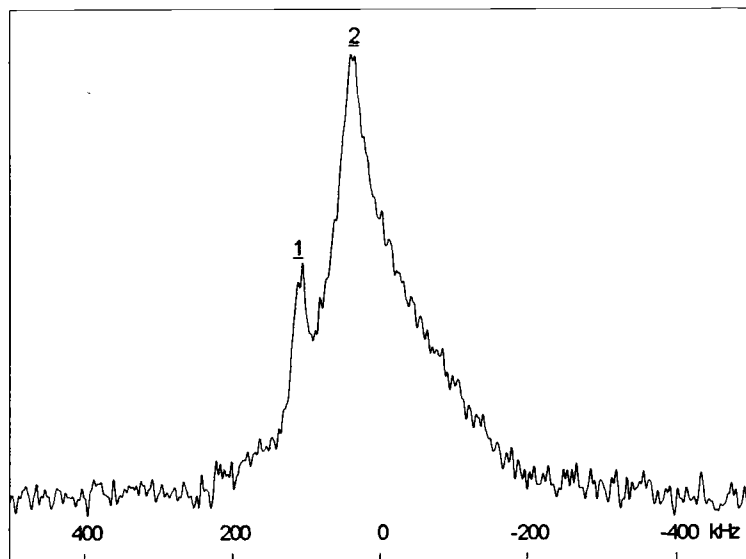


Figure 4-16: Spectrum of  $^{71}\text{Ga}$  in sample  $\text{Ga}(2)\text{O}(1)$ .

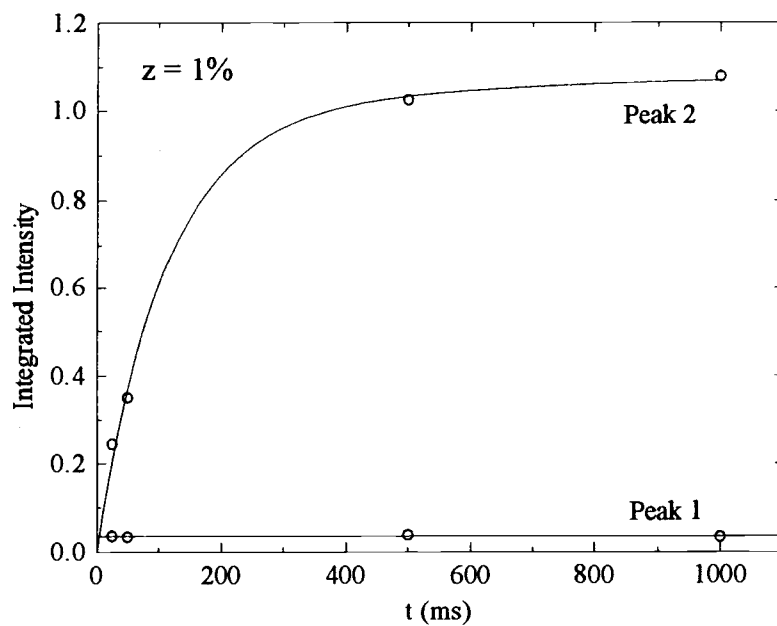


Figure 4-17: Integrated intensity of the individual peaks 1 and 2 vs. relaxation time  $t$ , for sample  $\text{Ga}(2)\text{O}(1)$ . Peak 1 is the site observed in series  $\text{Ga}(x)$ .

This “saturation-recovery” curve is a measure of the spin-lattice relaxation rate. In this case, the two lines were sufficiently resolved that it is possible to estimate the rate for each line separately. The data for site 2 was fit to magnetization recovery curve,

$$M(t) = M_{\infty} [1 - 0.1 \exp(-t/T_1) - 0.9 \exp(-6t/T_1)] \quad (4.3)$$

which gives  $(1/T_1)_{site2} = 1.5 \times 10^{-3} s^{-1}$ , and  $M_{\infty} = 1.09$ . The data indicates that site 1 is fully relaxed even for the shortest time ( $t = 25 ms$ ) so that  $(1/T_1)_{site1} > 40 s^{-1}$ , again consistent with measured values for site 1 in the stoichiometric series. The straight line fit for this site gives  $M_{\infty} = 0.04$ . The rate for site 1 is at least 2600 times faster than that of site 2.

## 4.4 Analysis and Interpretation

### 4.4.1 $Zn_{1-x}Ga_xO$

Bulk transport properties (section 4.2.1.1) suggest analysis of these samples as simple metals. Specifically, we seek to measure the Knight shift (e.g. the contribution from the total resonance shifts due to conduction electrons), and its relation to spin-lattice relaxation in the context of the theory of a simple metal (sections 2.2.2.2 and 2.3.1).

#### 4.4.1.1 *The Korringa Ratio*

The raw resonance shift data is a measure of the total resonance shift. Its contributions can be written,

$$S_{total} = \sigma_{iso} + K_{iso}, \quad (4.4)$$

where,  $\sigma_{iso}$ , and  $K_{iso}$  are the chemical shift and Knight shift respectively. The subscript *iso* indicates we are considering the isotropic contributions to the shift. (Note: As mentioned previously, anisotropies have the effect of producing well defined distributions in powder samples, from which the isotropic shift can be measured.)

Additionally, the measured spin-lattice relaxation rate will have contributions from both magnetic and quadrupolar interactions and therefore,

$$\left(\frac{1}{T_1}\right)_{\text{measured}} = \left(\frac{1}{T_1}\right)_{\text{magnetic}} + \left(\frac{1}{T_1}\right)_{\text{quadrupole}} \quad (4.5)$$

where  $\left(\frac{1}{T_1}\right)_{\text{magnetic}}$  represents the magnetic contribution<sup>†</sup>. Substituting into the

Korringa relation (2.52) gives,

$$\left[ \left(\frac{1}{T_1}\right)_{\text{measured}} - \left(\frac{1}{T_1}\right)_{\text{quadrupole}} \right]^{1/2} = \left(\frac{4\pi kT}{\hbar}\right)^{1/2} \left(\frac{\gamma_n}{\gamma_e}\right) (S_{\text{total}} - \sigma_{\text{iso}}). \quad (4.6)$$

$\sigma_{\text{iso}}$  is independent of the impurity concentration.

The quadrupole spin-lattice relaxation rate will vary as  $T^2$  above the Debye temperature, and will have an even stronger dependence below the Debye temperature.  $1/T_1$  temperature dependence in Figure 4-10 and Figure 4-11 is linear within experimental uncertainty. However, based on this data, an upper limit on the quadrupole contribution can be obtained. These results are  $\left(\frac{1}{T_1}\right)_Q^{69} < 8 s^{-1}$  for  $^{69}\text{Ga}$

in ZnO and  $\left(\frac{1}{T_1}\right)_Q^{27} < 0.16 s^{-1}$  for  $^{27}\text{Al}$ .

Figure 4-18 shows a plot of equation (4.6) where  $\left(\frac{1}{T_1}\right)_Q^{69} = 4 \pm 4 s^{-1}$  and

$\left(\frac{1}{T_1}\right)_Q^{27} = 0.08 \pm 0.08 s^{-1}$  is assumed.

---

<sup>†</sup> When dealing with excitation of the central transition, this separation of relaxation rate into magnetic and quadrupolar components is only approximate. This is because the functional form of the recovery curve is different for magnetic and quadrupolar relaxation. However, we know from the isotopic ratios that any quadrupole contribution has to be small, so use of equation (4.5) is appropriate for a small correction.

A linear least squares fit to the data for  $^{69}\text{Ga}$  yields,  $\sigma_{iso}^{69} = 220 \pm 80 \text{ ppm}$ .  $\sigma_{iso}^{27}$  for  $^{27}\text{Al}$  is in the range 50 to 100 ppm, however due to the small change in the resonance shift and spin-lattice relaxation a more precise value cannot be determined.

Focusing then on the  $^{69}\text{Ga}$  resonance, the Knight shift can now be determined by subtracting the chemical shift contribution from the total shift and is plotted in Figure 4-19. From the Knight shifts for the  $^{69}\text{Ga}$  nuclei, we can now calculate the corresponding Korringa relaxation rate according to equation (2.52). This is plotted in Figure 4-20, also included in the plot is the measured magnetic relaxation rate corrected for a quadrupole contribution.

Figure 4-20 exposes a strong correlation in the concentration dependence of the measured magnetic spin-lattice relaxation rate, and that predicted by the Korringa relation.

Also of interest is the value of the Korringa ratio, this is plotted in Figure 4-21 as a function of the impurity concentration. The straight line represents the constant 0.92 which is close to the ideal value of 1. This is strong evidence of nearly-free electron behavior where there is an absence of exchange effects and correlation.

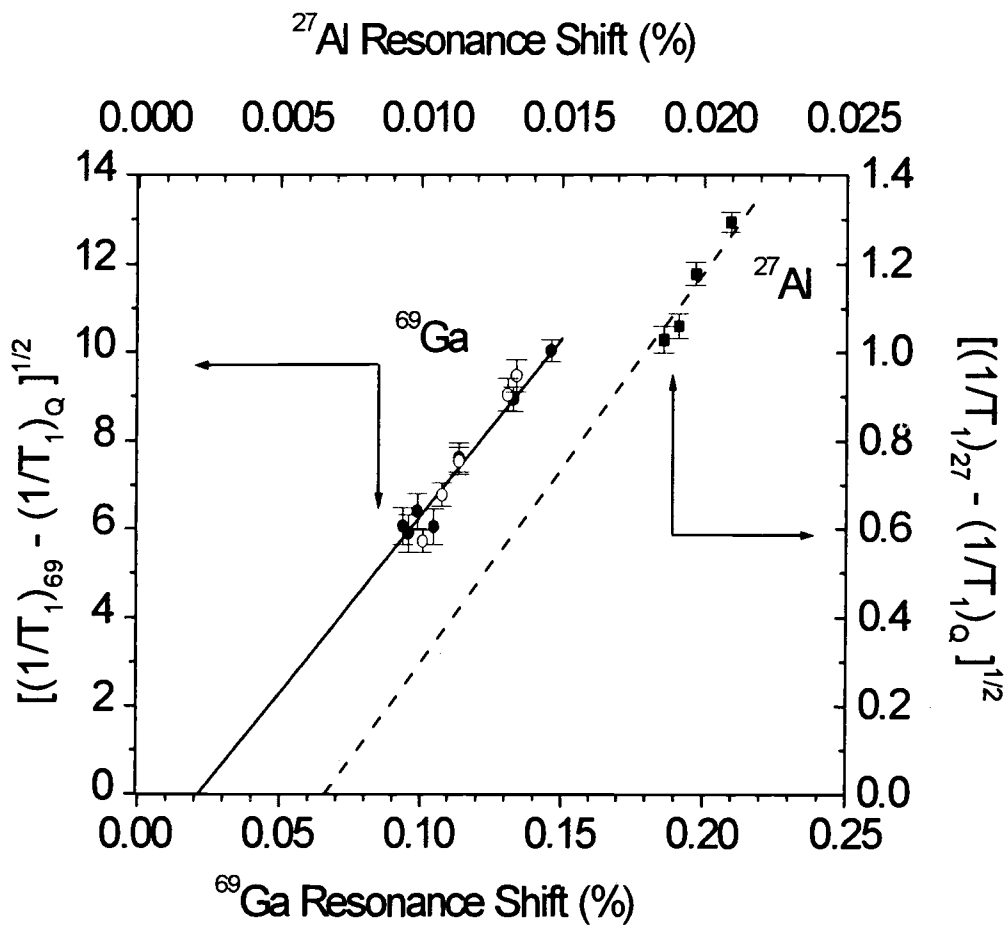


Figure 4-18: Square-root of the background-corrected spin-lattice relaxation rates versus total shift for  $^{69}\text{Ga}$  in sample series Ga(x) (solid circles) and series Ga(2)O(z) (open circles). Solid line represents linear least squares fit to the series Ga(x) and the dashed line is drawn with slope given by the Korringa Relation (2.52), for  $^{27}\text{Al}$ .

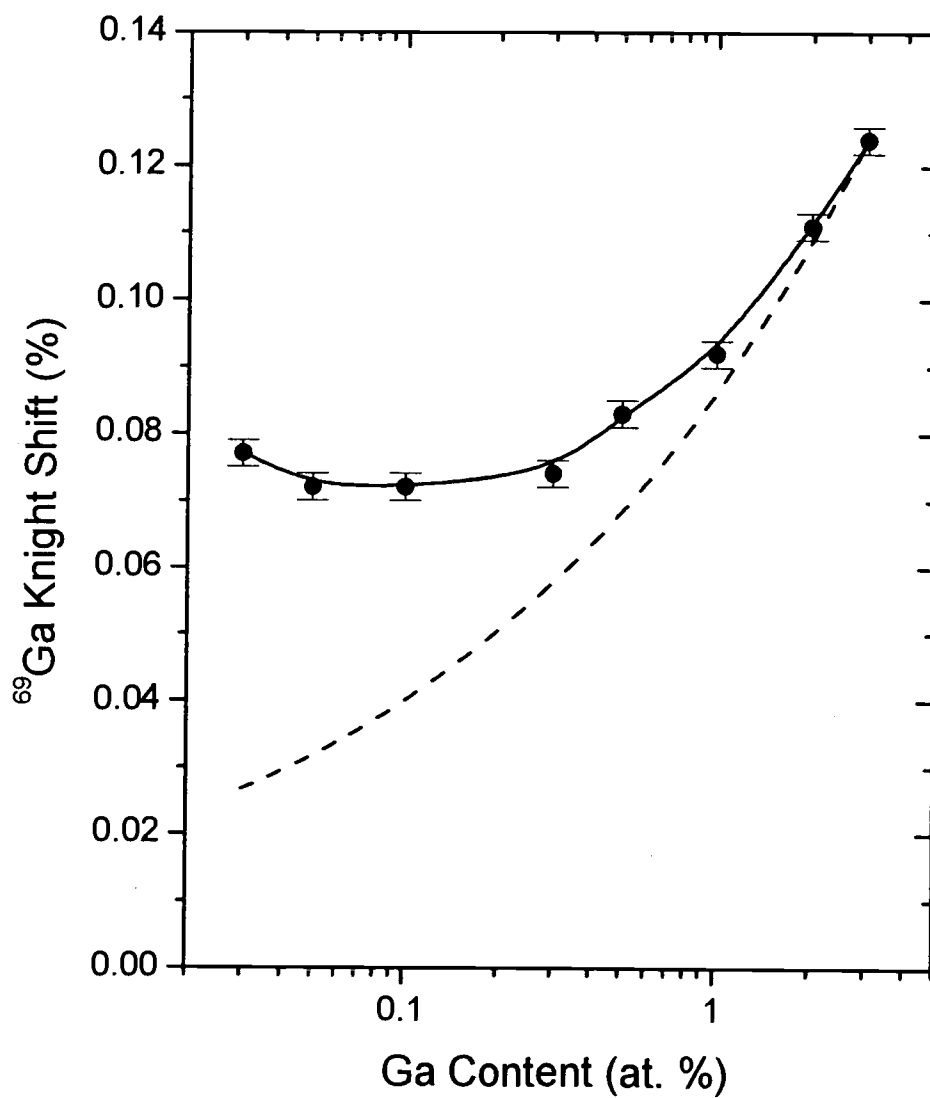


Figure 4-19:  $^{69}\text{Ga}$  Knight shift, corrected for chemical shift, versus nominal gallium concentration  $x$  for the stoichiometric series  $\text{Ga}(x)$ . Dashed line represents nearly-free-electron behavior  $K \propto x^{1/3}$ .

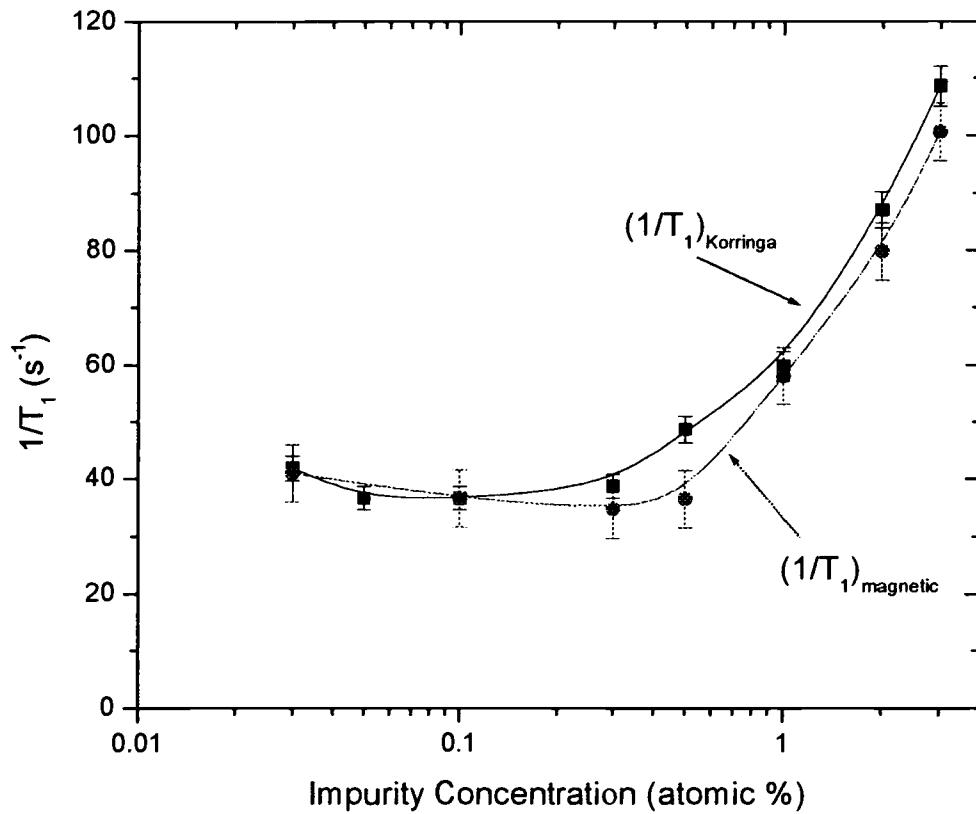


Figure 4-20: In the graph  $\left(\frac{1}{T_1}\right)_{Korringa}$  is the relaxation rate calculated from the measured Knight shifts and  $\left(\frac{1}{T_1}\right)_{magnetic}$  is the measured relaxation rate corrected for a quadrupolar contribution.

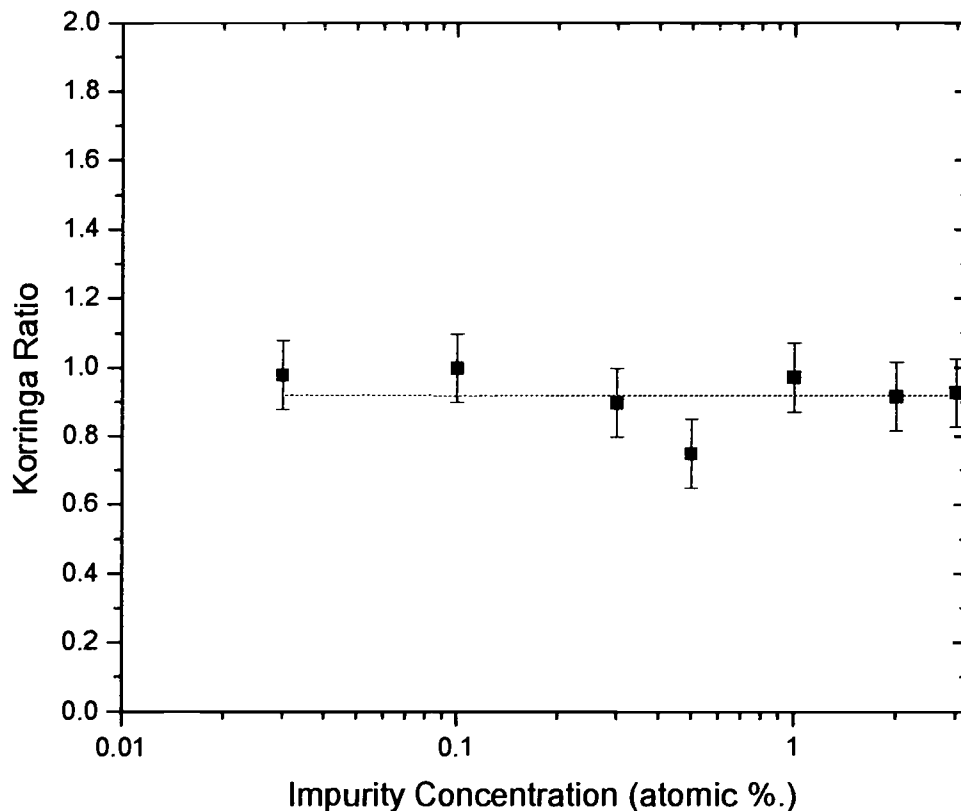


Figure 4-21: The Korringa ratio vs. impurity concentration for the series Ga(x). The error bars are relative. The absolute uncertainty is about  $\pm 15\%$ . The line represents a fit to a constant and has the value 0.92.

#### 4.4.1.2 The Knight Shift

The adherence to the Korringa relation, described in the previous section, suggest the free electron limit is an appropriate description of the electron system. Additionally, the temperature dependence on the spin-lattice relaxation rate indicates a degenerate electron system. As discussed in section 2.2.2.2, under these conditions the Knight shift is

$$K_{iso} = \frac{8\pi}{3} \chi_p \Omega \left\langle |\psi_s(0)|^2 \right\rangle_{FS}, \quad (4.7)$$

where, again,  $\chi_p$  is the Pauli spin paramagnetic susceptibility per unit volume given by,

$$\chi_p = \mu_B^2 \rho(E_F) \quad (4.8)$$

where  $\mu_B$  is the Bohr magneton and  $\rho(E_F)$  is the density of states at the Fermi level given by,

$$\rho(E_F) = \left( \frac{3m_{eff}}{\hbar^2} \right) \left( \frac{1}{3\pi^2} \right)^{3/2} n_e^{1/3}. \quad (4.9)$$

In the above expression  $m_{eff}$  is the conduction electron effective mass (accounting for the fact that the otherwise free electron is in a periodic potential) and  $n_e$  is the electron concentration. The Knight shift in (4.7) is shown in Figure 4-19 as the dashed line. The conduction band effective mass of  $0.38m_e$  in ZnO is assumed. Compared to the experimental results in the same figure, there appears an enhancement of the density of states that is largest at the low concentrations, decreasing as the concentration increases. The density of states converges to that of the parabolic conduction band of ZnO at the highest concentration.

This concentration dependence of the Knight shift, in conjunction with adherence to the Korringa relation even at low concentrations, indicates the development of an impurity band.

#### 4.4.1.3 The Hyperfine Coupling $\left\langle |\psi_s(0)|^2 \right\rangle_{FS}$

We can now calculate a value for the hyperfine coupling  $\left\langle |\psi_s(0)|^2 \right\rangle_{FS}$ . In S.I. units the Knight shift is written<sup>§</sup>,

---

<sup>§</sup> The motivation for this is simply the authors' familiarity with calculations performed in S.I. units.

$$K = \left(\frac{3}{2}\right) \chi_p \Omega \langle |\psi_s(0)|^2 \rangle_{FS} \quad (4.10),$$

and,

$$\chi_p = \mu_0 \mu_B^2 \rho(E_F), \quad (4.11)$$

where in the first equation  $\Omega$  is the atomic volume of the resonant species. For gallium in ZnO at 2.7 at. %, the gallium concentration per unit volume is  $n = 11.2 \times 10^{20} \text{ cm}^{-3}$ , and therefore  $\Omega = 1/n = 8.929 \times 10^{-22} \text{ cm}^3$ . Solving equation (4.10) for the hyperfine coupling gives,

$$\langle |\psi_s(0)|^2 \rangle_{FS} = \left(\frac{2}{3}\right) \frac{Kn^{2/3}}{\mu_0 \mu_B^2 \left(\frac{3m_{eff}}{\hbar^2}\right) \left(\frac{1}{3\pi^2}\right)^{3/2}}. \quad (4.12)$$

Assuming  $m_{eff} = 0.38$  for the conduction band of ZnO,  $\langle |\psi_s(0)|^2 \rangle_{FS} = 1.90 \times 10^{24} \text{ cm}^{-3}$ .

This value for the hyperfine coupling can be compared with ESR measurements in other gallium impurity systems. In ZnS<sup>22</sup>  $|\psi(0)|^2$  was measured to be  $3.83 \times 10^{25} \text{ cm}^{-3}$ , and in NaCl and KCl<sup>23</sup> values of  $5.87 \times 10^{25} \text{ cm}^{-3}$  and  $5.57 \times 10^{25} \text{ cm}^{-3}$  were obtained respectively for <sup>69</sup>Ga. However, in all of these systems the result of gallium was a highly localized electronic state. In the present ZnO the are highly extended particularly at the highest impurity concentrations, and therefore we expect a smaller coupling constant.

#### 4.4.2 Zn<sub>0.98</sub>Ga<sub>0.02</sub>O<sub>1+z</sub>

As stated previously, two distinct classes of <sup>69</sup>Ga are observed in this sample series unambiguously for  $z > 0$ . It is noted that the time domain spin-echoes in Figure 4-12 and Figure 4-13 leave open the possibility of a second site for  $z < 0$ . However, for this range of  $z$ , the narrow peak indicating the second site is also quantitatively consistent with a contribution from the satellite transitions for a quadrupolar nucleus. One class of site, designated site 1, is identified as the same substitutional gallium site,  $Ga_{zn}$ , as that seen in the stoichiometric samples.

This is based on the consistency of the resonance shifts, spin-lattice relaxation, and line-width experimental results.

The second class of gallium site observed, site 2, is characterized by a smaller resonance shift (0.035%) compared to site 1 (0.08%) in the same sample.

Additionally, the spin-lattice relaxation rate for this site is several orders of magnitude smaller than that of the site  $\text{Ga}_{\text{zn}}$ , indicating the dominant relaxation mechanism is not magnetic in origin. Line width comparisons indicate site 2 is highly distorted compared to site 1.

It is therefore reasonable to assume that the carrier concentration is determined by the number of substitutional gallium sites. This is also supported by bulk transport data where the conductivity decreases with increased oxygen content, and therefore a decrease in the fraction of substitutional sites. The fraction of substitutional sites ( $f_s$ ) versus oxygen content can be estimated by the spin-echo data in Figure 4-12, where

$$f_s = \frac{\text{contribution to the total amplitude from narrow peak}}{\text{total amplitude}} \quad (4.13)$$

Assuming  $f_s$  is equivalent to the carrier concentration, the same analysis as that in the stoichiometric series is performed. The result is represented by the open circles in Figure 4-18. The data indicate the same Korringa-like correlation as observed in the stoichiometric samples.

Again, as in the previous analysis, the Knight shift can be extracted, and this is shown in Figure 4-22, where the dashed line represents  $K \propto f_s^{1/3}$ , nearly free electron

behavior. The data agrees qualitatively with that of the stoichiometric material.

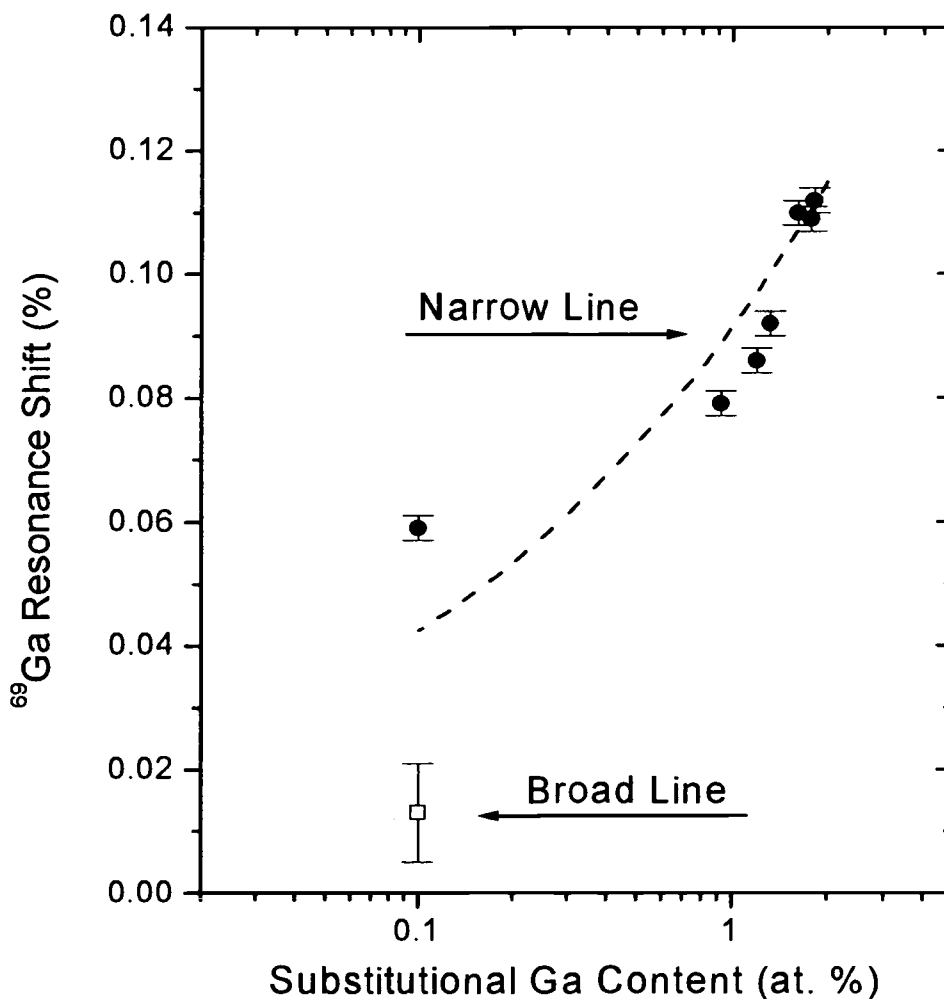


Figure 4-22:  $^{69}\text{Ga}$  Knight shift of nonstoichiometric samples  $\text{Zn}_{0.98}\text{Ga}_{0.02}\text{O}_{1+z}$ , corrected for chemical shift, versus substitutional gallium content  $x_s$  determined from spin-echo shapes. Dashed line represents nearly-free-electron behavior,  $K \propto x_s^{1/3}$ . The corrected Knight shift value of the broad line component is also shown (open square).

The three data points with the largest  $K_{shift}$  are from samples  $\text{Ga}(2)\text{O}(-1.2)$ ,  $\text{Ga}(2)\text{O}(-0.5)$  and  $\text{Ga}(2)$  (the sample from the stoichiometric series that would correspond to

Ga(2)O(0.0)). Within experimental observation, these are essentially the same data point, since the second distorted gallium site is not unambiguously observed in these samples. Therefore, this indicates good quantitative agreement between the stoichiometric and non-stoichiometric material.

A possible explanation for the discrepancy for smaller  $f_s$  could be systematic experimental error, rooted in the vast difference of the spin-lattice relaxation rates for the substitutional and distorted gallium sites. In determining  $f_s$  from the spin-echoes, we assume both sites are fully relaxed. This is likely true for the substitutional site, however, this may not be the case for the distorted site, characterized by a much slower rate. This scenario would tend to over estimate the value of  $f_s$ . Due to the experimental effort involved, no attempt was made to better characterize the distorted site, and re-design the spin-echo experiment based on this. Returning now to the distorted site 2. As indicated previously, this site appears to be de-coupled from conduction electrons. The broad, featureless line gives now indication of the structure of this site. A possible candidate is a doubly-charged oxygen interstitial complexed with two  $\text{Ga}^{3+}$  according to the reaction  $2\text{Ga}^{3+} + \text{O} + 2e^- \rightarrow \text{Ga}_2\text{O}_i^{2-}$ . The low relaxation rate essentially rules out the possibility of paramagnetic centers such as  $\text{Ga}^{3+}$  complexed with a singly charged oxygen interstitial.

## 4.5 Conclusions

In the stoichiometric materials,  $\text{Zn}_{1-x}\text{Ga}_x\text{O}$ , comparison of the  $^{67}\text{Zn}$  and  $^{69}\text{Ga}$  NMR spectra for  $x = 0.0$  to 2.0 atomic percent, indicates that impurity gallium is substitutional for zinc. Spectra also indicate the effect of introducing gallium is a lowering of the axial symmetry at the zinc site without a significant change in the magnitude of the electric field gradient. Comparison of spin-lattice relaxation rates for the  $^{69}\text{Ga}$  and  $^{71}\text{Ga}$  isotopes shows that the dominant relaxation process is magnetic in origin even at low impurity concentrations. Additionally, the relaxation rate is proportional to the temperature, consistent with nuclear moments coupled to

degenerate electrons. This is consistent with temperature dependent conductivity studies<sup>15</sup> from 4.2K to room temperature, which indicate that the samples are in the highly doped regime for impurity concentrations down to 0.1 atomic percent. Gallium Knight shift and spin-lattice relaxation rate data both increase with increasing impurity concentration for  $x > 0.5$  at. %, however, are nearly independent of concentration for  $x < 0.5$  at. %, representing a deviation in the Knight shift away from free electron behavior ( $K \propto x^{1/3}$ ). At all concentrations, the Knight shift and spin-lattice relaxation rates remain correlated by the Korringa Relation for simple metallic behavior. The deviation in the Knight shift concentration dependence at the lower concentrations, combined with adherence to the Korringa relation and conductivity data, imply the formation of an impurity band that eventually merges with the parabolic conduction band of the host ZnO lattice at the highest concentrations.

Experimental NMR results for  $^{27}\text{Al}$  in the series  $\text{Zn}_{1-x}\text{Al}_x\text{O}$  are qualitatively the same as for  $^{69}\text{Ga}$ . However, the much smaller effects observed did not warrant quantitative analysis.

$^{69}\text{Ga}$  NMR results were obtained in the non-stoichiometric materials,  $\text{Zn}_{0.98}\text{Ga}_{0.02}\text{O}_{1+z}$ , for  $z = -1.2$  to 1 at. %. In these samples the gallium metal content is held constant at 2 at. %. Samples spanned a range from oxygen deficient ( $z < 0$ ) to excess oxygen ( $z > 0$ ). For the excess oxygen samples, 2 sites for gallium are observed. One site is identified as the substitutional site observed in the stoichiometric series. This conclusion is based on comparisons of the spectra, Knight shift, and relaxation rates between the stoichiometric and non-stoichiometric samples. The spectrum for the second site indicates a much more highly distorted site than the substitutional site. The relaxation rate for the second site can only be estimated primarily due to a small signal to noise ratio, and is only readily observed in the frequency domain for the most oxygen excess sample. The rate is estimated to be several orders of magnitude smaller for this second, highly distorted site. Knight shift and relaxation rates for the substitutional site decrease with increasing oxygen content. This is also consistent

with conductivity data<sup>15</sup> which show a decrease in the conductivity with increasing oxygen. These facts in conjunction with the long relaxation rate of the distorted site (indicating essentially no magnetic coupling) points toward this site as representing a diamagnetic carrier trap.

## Bibliography

---

- <sup>1</sup> P.P. Man, *Quadrupole couplings in Nuclear Magnetic Resonance, General*, in Encyclopedia of Analytical Chemistry, (John Wiley & Sons Ltd, Chichester, 2000), pp. 12224-12265
- <sup>2</sup> G. C. Carter, L. H. Bennett, D. J. Kahan, *Metallic Shifts in NMR*, Progress in Materials Science, 20, 1977
- <sup>3</sup> Knight, W. D., Solid State Physics, Vol. 2, p. 93, (Seitz, F. and Turnbull, D., eds.), Academic Press, New York (1956)
- <sup>4</sup> C.P. Slichter, *Principles of Magnetic Resonance*, third edition, Springer, Berlin Heidelberg New York, 1990
- <sup>5</sup> J. Korrying, Physica 16, 601 (1950)
- <sup>6</sup> Fukushima, Eiichi, and Roeder, Stephen B. W., (1981) *Experimental Pulse NMR: A Nuts and Bolts Approach*, Addison-Wesley, New York
- <sup>7</sup> Actually, in practice, the frequency mixing is often a multi-stage process involving more than one intermediate frequency. However, this is only a performance issue and is not important conceptually.
- <sup>8</sup> Solomon, I., 1958, Phys. Rev., 110, 61
- <sup>9</sup> Bonera, G., and Galimberti, M., 1966, Solid St. Commun., 4, 589
- <sup>10</sup> Bonera, G., Avagadro, A., and Borsa, F., 1968, Phys Rev., 165, 391
- <sup>11</sup> Weisman, I.D., and Bennett, L. H., 1969, Phys. Rev., 181, 1341
- <sup>12</sup> Warren, W. W., and Norberg, R. E. 1967, Phys. Rev., 154, 277
- <sup>13</sup> V. Korthius, N. Khosrovani, A. W. Sleight, N. Roberts, R. Dupree, W. W. Warren Jr., Chem. Mat. 7, 412, (1995).
- <sup>14</sup> Courtesy of Bruker Spectrospin, GmbH.
- <sup>15</sup> R. Wang, A. W. Sleight, and D. Cleary, Chem. Mater. 8, 433 (1996)
- <sup>16</sup> This represents the solubility limit of Gallium in ZnO<sup>15</sup>.
- <sup>17</sup> R. Wang, Laura L. H. King, A. W. Sleight, J. Mater. Res. 11, 1659 (1996)
- <sup>18</sup> EMPA results indicate a solubility limit of 2.7%.
- <sup>19</sup> Fritzsche, H.; Cuevas, M. Phys. Rev. 1960, 119, 1238

---

<sup>20</sup> T. J. Bastow and S. N. Stuart, *Phys. Status Solidi B* 145, 719 (1988)

<sup>21</sup> In fact, if this is true, the width and position of site 2 are really not known. What is reported is simply what is observed within the pulse spectrum at one frequency.

<sup>22</sup> A. Rauber and J. Schneider, *Phys. Status Solidi* 18, 125 (1966)

<sup>23</sup> P.G. Baranov and V.A.Khramtsov, *Sov. Phys. Solid State* 20, 1080 (1978)